universität wien

MASTERARBEIT / MASTER'S THESIS

Titel der Masterarbeit / Title of the Master's Thesis

"A methodological approach to the thermochronology of the Winnebach migmatite."

verfasst von / submitted by

Michael Oester, BSc

angestrebter akademischer Grad / in partial fulfilment of the requirements for the degree of

Master of Science (MSc)

Wien, 2017 / Vienna, 2017

Studienkennzahl lt. Studienblatt / degree programme code as it appears on the student record sheet:	A 066 615
Studienrichtung lt. Studienblatt / degree programme as it appears on the student record sheet:	Erdwissenschaften
Betreut von / Supervisor:	Ao. Univ. Prof. Mag. Dr. Urs Klötzli
Mitbetreut von / Co-Supervisor:	Mag. Dr. Eva Klötzli-Chowanetz

Contents

List of Figures

List of Tables

Acknowledgements

I would like to acknowledge the support and encouragement I received during the process of writing this thesis. This work stands on many shoulders, many of whom will go unnamed despite my gratitude. However, I would like to thank the following people in particular:

My advisors, Eva and Urs. Thank you for many long and productive discussions and for answering countless questions, for giving me space and time to follow my ideas and encouraging me to think these through. I am very grateful for everything I have learned from you.

My officemates and other colleagues, who spent many coffee- and lunch-breaks with me, and for lending an understanding ear to tales of my frustration. Special thanks to Bernhard, for being an excellent travelling companion.

All my friends, for their encouragement and assistance with many things, not only relaxation. I owe a special 'thank you' to Thomas 'Three-names' Pichler, for proofreading and corrections.

Finally, my family, for all their support and patience, and for trying their very best to be interested in my work.

1. Introduction

The Ötztal Complex (ÖC), located in Tyrol, western Austria, and extending into eastern Switzerland and northern Italy, is a polymetamorphic basement unit of the Austroalpine (Hoinkes et al. 1972; Klötzli-Chowanetz et al. 1997; Thöni 1999). Within this unit, at least three phases of metamorphism can be observed. The youngest, an Eo-alpine overprint shows conditions from greenschist-facies in the north-west of the complex, up to amphibolite-facies in the south-east (Hoinkes et al. 1991). These south-eastern parts have shown mica cooling ages of 90–70 Ma, while micas in the north-east still show Variscan ages. (Schmidt et al. 1967, Thöni 1981).

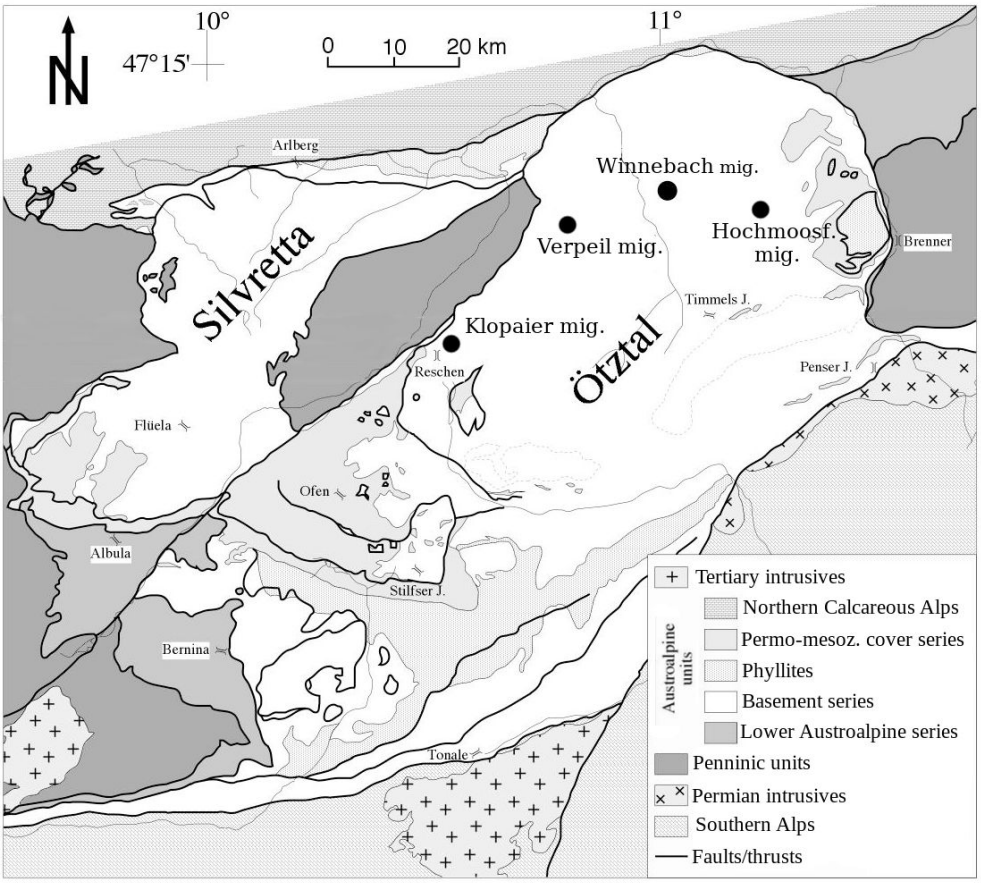

Figure 1.1.: Tectonic map of the Ötztal Complex. Modified after Klötzli-Chowanetz 2001. Coordinates for the migmatites are given in Appendix A

The Variscan metamorphism, which is the most commonly visible, generally reached amphibolite-facies (Hoinkes and Thöni 1993). The eclogitization within the Ötztal metabasite suite at an age of 360–350 Ma is attributed to an early Variscan phase (Miller and Thöni 1995).

Evidence for pre-Variscan metamorphic history is mostly limited to Cambrian ages of gabbros, which are interpreted as protoliths of eclogites (Miller and Thöni 1995), Ordovician magmatism in the central and western ÖC (Bernhard et al. 1996, Schmidt et al. 1967), and several small bodies of migmatites (Figure 1.1, coordinates are given in Appendix A):

- Hochmoosferner migmatite, a very narrow band within the Stubai valley, located just below the glacier "Hochmoosferner" (Schindlmayr 1999).
- Verpeil migmatite in the Kauner valley, described as stromatic, and stands in contrast to the other migmatites separated into leuco- and melanosome (Bernhard 1994).
- Winnebach migmatite in the central Ötz valley, the main area of interest for this thesis. (Figure 1.2)
- Klopaier migmatite, in the Area of the Reschenpass, consists of five lenses of anatectic metasediments (Schweigl 1993). Like the Winnebach-migmatite, it is not separated into leuco- and melanosome, but is a Schollen-migmatite (Klötzli-Chowanetz 2001).

The Winnebach migmatite is a large lenticular migmatite-body in the ÖC with a size of approximately 25 km^2 (Klötzli-Chowanetz 2001). It is surrounded by metasedimentary gneisses, which are also interpreted as the protolith (Hoinkes et al. 1972; Klötzli-Chowanetz 2001; Schindlmayr 1999). The migmatite is of granodioritic bulk composition (Hoinkes 1973). The whole migmatite body was only peripherally touched by Variscan metamorphism, where it has a distinct schistosity. As there is no visible post-anatectic deformation over the whole migmatite, the anatectic event was originally thought to be Variscan, but single micas in the central migmatite give an age of approximately 460 Ma, which shows the migmatite to be of pre-Variscan age (Chowanetz 1991). A detailed study of zircons from the migmatite and the surrounding gneisses revealed a population of small, spheroidal zircons to be present in the migmatite only. These anatectic zircons yield a Cambro-Ordovician concordia U-Pb age of 490 ± 9 Ma (Klötzli-Chowanetz et al. 1997).

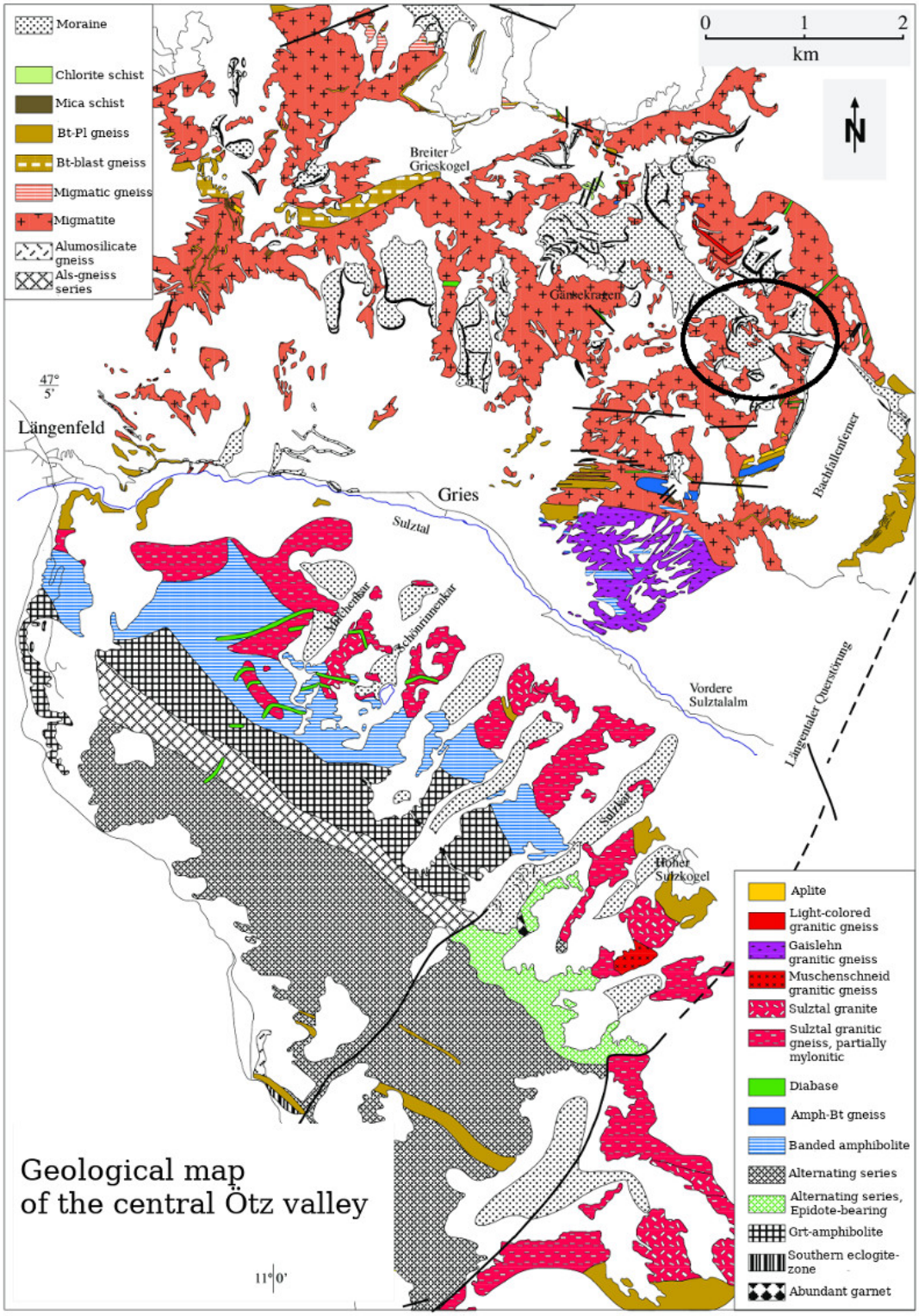

Figure 1.2.: Geological map of the central Ötz valley. North of Sulz valley: Chowanetz 1991; South of Sulz valley: Hoernes and Hoffer 1973. Modified after Klötzli-Chowanetz 2001. Sample locations within black ellipse, for detailed locations see Table A.2.

1.1. Objectives

The objective of this thesis is set to provide further detailed insights into the metamorphic history of this polymetamorphic migmatite. Special focus was laid on possible different melt generations, and the wide range of textures produced by the anatexis.

To this purpose petrological investigations where performed on the chemistry of different mineral phases, using Electron Microprobe Analysis.

In-situ U-Pb dating of accessory phases was applied to provide further data on high temperature metamorphic events recorded in this unit.

The Ti-in-zircon geothermometer was tested for practicality and applicability for this case, and to help provide a better estimate for anatectic temperatures.

1.2. Definitions of terms used

There are numerous models concerning the process of anatexis. Typical of migmatites is the differentiation of a pre-anatectic material into leucocratic zones, with a mineralogy of mainly quartz and feldspar (leucosomes), and darker melanocratic areas, which are comprised of predominately mafic minerals(melanosomes). In-between these two in respect to colour, lies the so called mesosome (Mehnert 1968). In older models of migmatization this division is also applied to age differences: The mesosome was regarded as the undifferentiated protolith and thus identified as the paleosome, while the melano- and leucosomes were interpreted as the products of differentiation by partial melting (Mehnert 1968). However, since the beginning melt-processes continuously alter the protolith chemically, texturally as well as in its mineralogy, in most cases it does not seem beneficial (nor is it possible in some cases) to try to identify a paleosome.

Thus, newer models refer to the processes as differentiation of a protolith into restite and melt, by partial anatexis, which leads to a partial segregation of restite and melt (Kriegsman 2001). A partial back-reaction between segregated melt and adjacent restite forms the leucosome and melanosome, respectively, while the mesosome is formed by a partial back reaction between unsegregated melt and restite. However, melt loss, or decompression after the thermal peak might prevent reaction reversal, thus leading to new reactions on the retrograde path (Brown 2002).

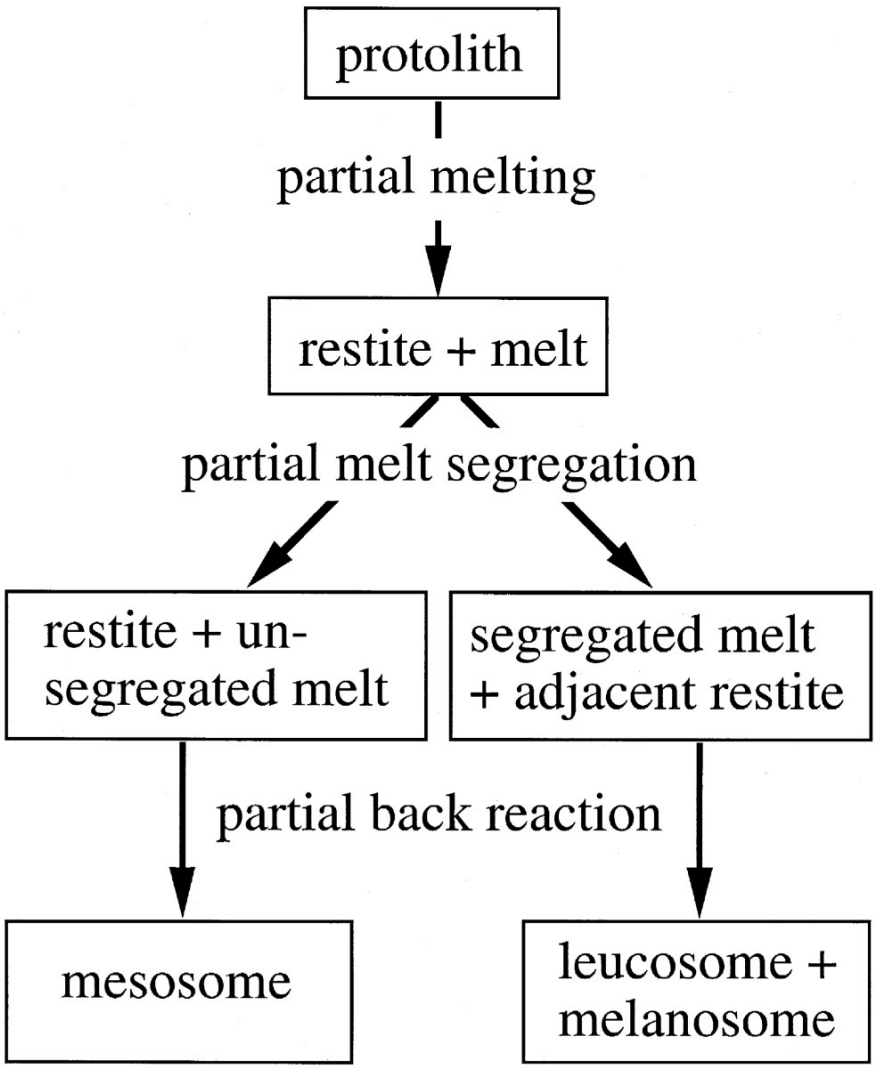

Figure 1.3.: Flowchart of Kriegsman's model of migmatite evolution (Kriegsman 2001)

2. Fieldwork

The investigated outcrops are all in the central part of the migmatite, where the rocks are strongly abraded and polished by the glacier "Bachfallenferner", which has now retreated further upwards. The smooth, relatively little weathered surface provides an excellent opportunity to study the migmatite in close detail. As there are large coherent surfaces, spatial distribution of lithologies and textures can be observed quite well.

The smoothness of the surfaces presents one problem, however: Traditional sampling methods using hammer and chisel are impossible. To overcome this problem, a battery-powered angle grinder with a diamond blade was used to cut grooves into the rock, after which the block can be levered out using hammer and chisel (Figure 2.1).

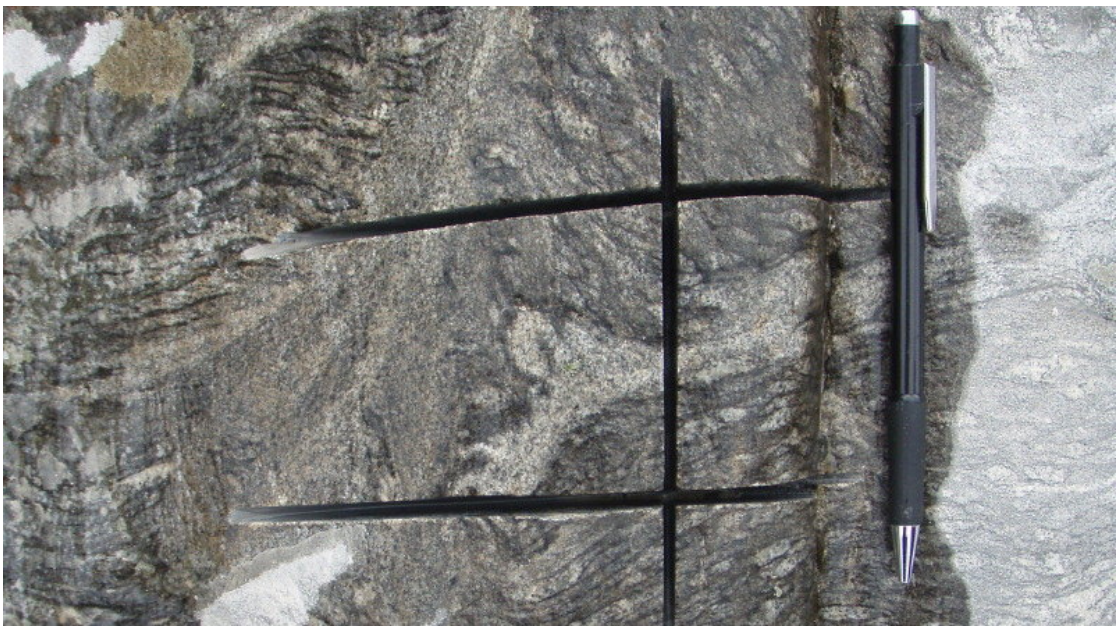

Figure 2.1.: Sampling using a battery-powered angle grinder. The block inbetween the grooves and the fracture can then be levered out using hammer and chisel. Sample W1412

2.1. Lithologies

The process of partial anatexis transforms the protolith — a metagreywacke-series (Hoinkes et al. 1972) — into a variety of distinguishable lithologies. Not all lithologies are affected to the same degree by melting reactions. While some are only texturally altered (schollen), others disintegrate completely, reaching a chemical differentiation. Even similar textures can be made of different lithologies, e.g. schollen. There is no systematic spatial distribution of the lithologies in the migmatite body on a bigger scale. The wide range of lithologies results most likely from a varying chemical composition of the protolith, which leads to different rates of melt production at the anatexis.

2.1.1. Biotite-Plagioclase Gneiss

Bt-Pl gneisses occur in the central migmatite mostly as fine-grained, finely laminated schollen (Figure 2.2). At the margins these are lightly to strongly altered by melt-producing reactions. Characteristic are alternating layers of quartz and feldspar with biotite. Lighter coloured schollen often exhibit expansion of the felsic layers, which leads to a dissipation of the texture. The size of the schollen is highly variable, and ranges from few centimetres to contiguous belts several metres of length, which are often strongly folded. The folding corresponds to the internal foliation, the tectonic event leading to these structures is unclear.

Figure 2.2.: Biotite-Plagioclase Scholle, showing boudinage

Figure 2.3.: Folded band of calcsilicate

2.1.2. Calcsilicate

Seemingly not reacting with their surroundings, calcsilicates occur mostly as folded colourful bands within the migmatite (Figure 2.3). The colours – ranging from pale blue, over green to pinkish red – can also be arranged zonally. Since it is a very fine-grained lithology, the mineralogy cannot be determined macroscopically. Typically they are very hard and resistant to weathering, especially compared to the surrounding lithologies. Furthermore they often exhibit boudinage, and are sometimes enveloped

by a fine-grained leucocratic layer. The absence of thinning of limbs, as well as thickening of fold-hinges might indicate deformation in a low-viscosity environment (Park 1997).

2.1.3. Biotite Schist

In addition to the lightly coloured Bt-Pl gneisses, there are dark biotite schists to be found. These are very fine-grained, and mostly of smaller size (Figure 2.4). Normally they include single layers of coarse-grained leucocratic material. Frequently associated with these leucocratic layers are often big greenish mineral phases. Ohnesorge 1905 interpreted these in analogy to a different location as possible pinites (white mica and chlorite pseudomorphs after cordierite). At times they are surrounded by a biotite selvedge. Moreover there are also morphologically similar blue phases in these zones. These are very soft, which causes them to predominately exhibit strong glacial striation.

Figure 2.4.: Biotite Schist with coarse-grained leucocratic layers

Figure 2.5.: Schollen cut by leucocratic veins forming a network

2.1.4. Melt-Network and Homogeneous Neosome

In-between the schollen or even cutting these a network of veins is visible (Figure 2.5). The scale of these networks varies strongly and ranges continuously from few centimetres to metre-sized dykes. Smaller veins show a composition of mainly quartz and feldspar, whereas bigger dykes contain biotite as well. There are examples where granitic dykes cut through haplogranitic ones, and vice versa, therefore no clear chronological order can be established from field relations (Figure 2.6). It has to be noted that even though the term ”haplogranitic” stems from experiments in the quartz-albite-orthoclase system, it is used in this context as a term for the field-description of these veins consisting macroscopically of only quartz and feldspar.

The granodioritic homogeneous mass within the migmatite was previously labelled “homogeneous neosome” (Hoinkes et al. 1972). The schollen are surrounded by this

matrix. In addition, schollen can sometimes be seen to be suspended in discordant dykes of homogeneous neosome (HN, Figure 2.7).

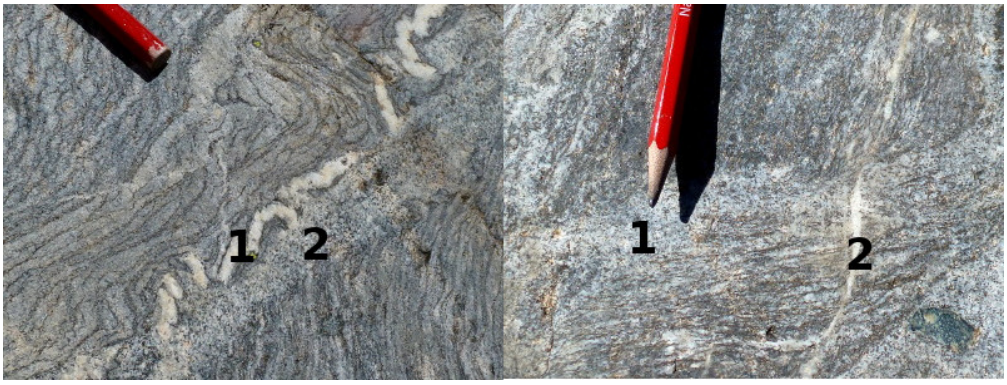

Figure 2.6.: Different chronological orders of veins, numbered by order of appearance.

Figure 2.7.: Schollen within dyke of homogeneous neosome

2.2. Textures

In addition to lithological differences, the partial anatexis also leads to a multitude of different textures. Notably, there is no spatial separation of these textures on a larger scale. As is the case with different lithologies, textures can not be allocated to specific zones within the migmatite.

2.2.1. Schollen

Figure 2.8.: Dissipation of metamorphic foliation within Bt-Pl scholle

Schollen within the migmatite consist of either bt-pl gneiss, bt-schist or calcsilicate, with basitic schollen being notably absent. Frequently they exhibit folding of the metamorphic foliation. Along the margins of the schollen, this foliation is often times beginning to dissipate (Figure 2.8). In some cases this leads to complete dissolution of the schollen within the neosome, even though single layers can still remain coherent and remain as small fragments. These zones of dissolving schollen were previously referred to as "inhomogeneous neosome" (Hoinkes et al. 1972). An example for this phenomenon is the spotted gneiss, described by Bidner 1989, which results from severed Bt-layers (Figure 2.9). However, other processes might be responsible for these textures in combination with the dissipation of the schollen. The coarse grain-size of the spotted gneiss might also be a result of a coarse-grained protolith, such as the directly adjacent Gaislehn granite gneiss.

Figure 2.9.: Spotted gneiss, as described by Bidner 1989, progressive breaking up of Bt-layer from left to right

Figure 2.10.: Bubbles textures

2.2.2. Bubbles

Furthermore, some schollen exhibit round to lenticular structures, where instead of whole layers being widened, the expansion here is strongly localized (Figure 2.10). These mostly white patches consist mainly of quartz and feldspar, sometimes they contain biotite. More often, however, they are surrounded by a biotite-rim at the border to the Scholle. The size is normally limited to a few centimetres.

2.2.3. Networks

As mentioned before, dykes of haplogranitic to granitic composition exist within the migmatite body, within or in-between the schollen. On a small scale these are often connected to layer-concordant dykes, or seem to be rooted in bigger bubbles. Emanating from there, we find complex, three-dimensional networks of dykes cutting the schollen (Figure 2.11). Small haplogranitic dykes often exhibit a biotite-rim, similar to melt bubbles. With increasing size the composition moves gradually to a granitic system, with increasing biotite content within the dyke itself, not only on its margins.

Figure 2.11.: Melt networks cutting through schollen

2.2.4. Homogeneous Neosome

With the increasing size of dykes and in conjunction with a compositional shift to a granodioritic chemistry, large areas (several m^2) of massive material start to appear. These areas are often difficult to recognize as dykes because of their size. Schollen are embedded into this granodioritic matrix. Even though they are sometimes locally oriented in a common direction, no preferred orientation is visible on a larger scale. The matrix adjoining the oriented schollen often exhibits flow structures (Figure 2.12).

A gradual transition of dissolving schollen to homogeneous neosome makes a classification difficult. The name "homogeneous neosome" stems from the description of Hoinkes et al. (1972).

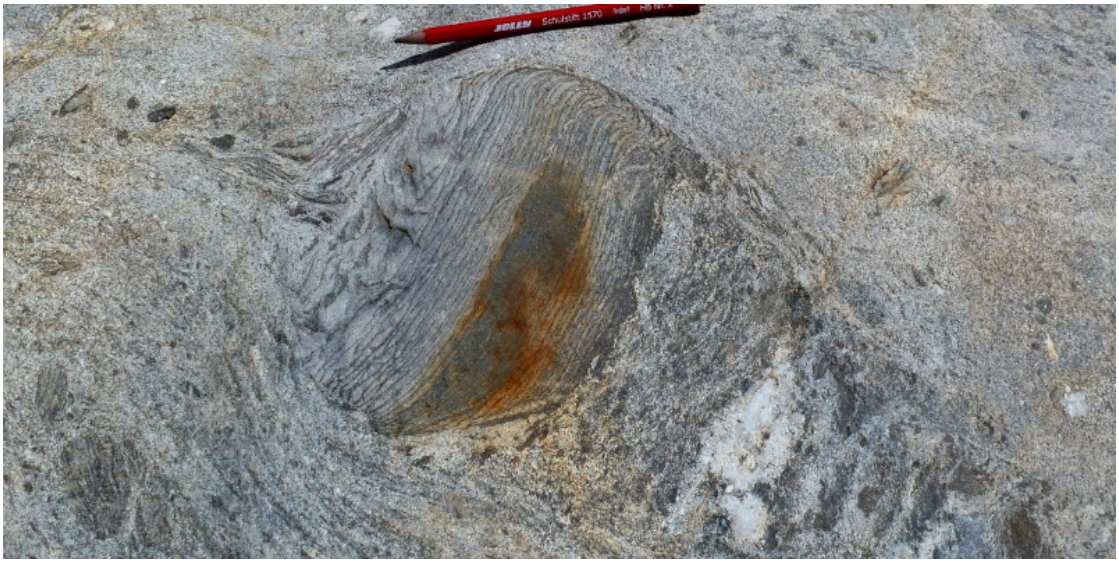

Figure 2.12.: Flow structures within Homogeneous Neosome around a scholle

3. Petrology

3.1. Microscopic Petrography

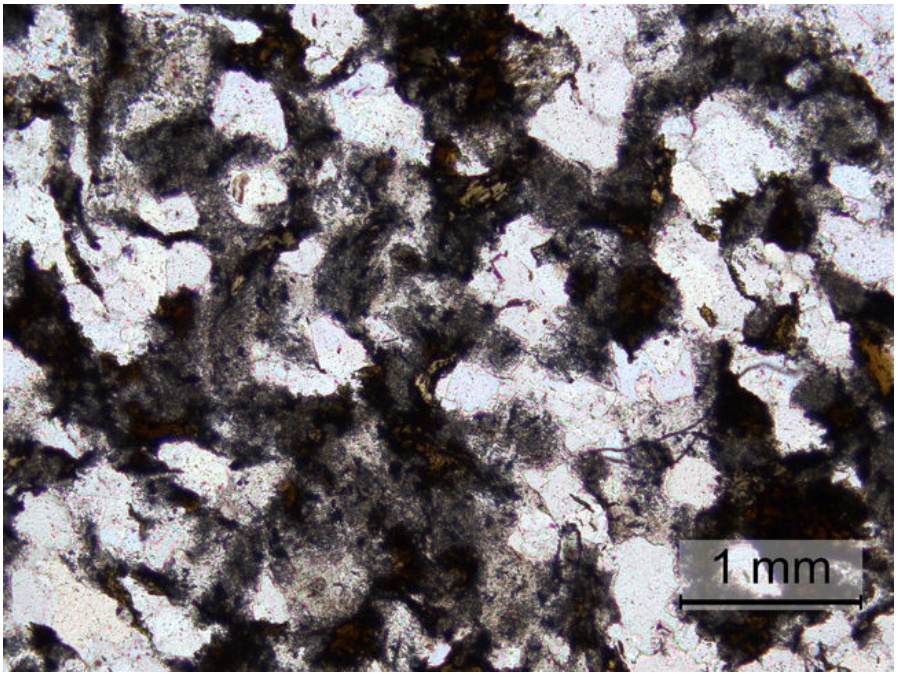

Figure 3.1.: Microscopic texture of neosome: Fine-grained matrix in-between coarser grains of plagioclase, quartz and biotite. Fibrous patches were identified as kyanite by Klötzli-Chowanetz (2001). (Sample W1412Na3, PPL)

What distinguishes the migmatite from the surrounding paragneisses – apart from the absence of visible strain – are patches of granular, fine-grained plagioclase in-between bigger grains (Figure 3.1) (Klötzli-Chowanetz 2001; Schantl 1972). Microscopy of thin-sections reveals unoriented grains in the central parts of the migmatite-body. The fine-grained patches consists mainly of plagioclase and white mica. Occasionally patches rich in alkali feldspar occur. The patchy appearance is further amplified by extremely fine-grained, finely distributed minerals, which can colour patches brown (biotite), or greenish-gray. Often the latter colour is combined with a fibrous appearance. Klötzli-Chowanetz (2001) identified fibrous patches like these as fine-grained aluminosilicate (Figure 3.1).

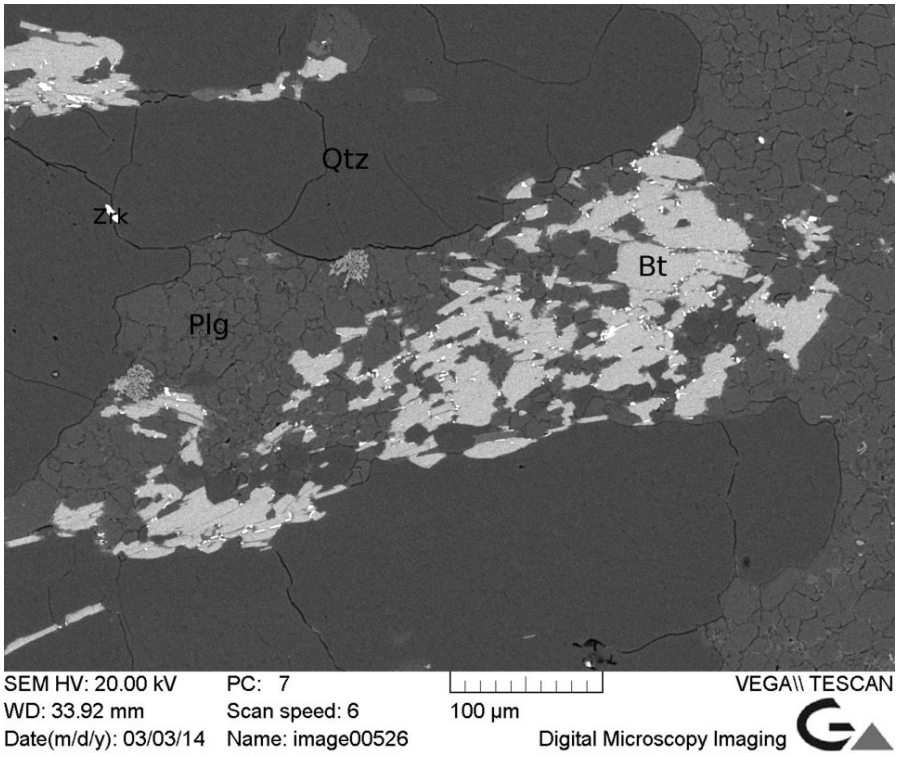

Figure 3.2.: SEM-image of biotite-plagioclase interface with fine-grained ilmenite (Sample W8877)

Quartz and both feldspars also exist as bigger grains (approximately 0.3-1mm), as do biotite and white mica. Both of the latter ones exhibit highly irregular forms, namely dissolution textures. Only small, long prismatic crystals of white mica occur idiomorphically. Biotite often occurs in big heaps, which sometimes can be recognized as remnants of metamorphic layering. In these remnants, a common orientation is locally preserved. Biotite heaps bring to mind the selvedges consisting of biotite and sillimanite described by Spear et al. (1999), which are described as replacing garnet and cordierite. In the case of these samples, however, there is little to no aluminosilicate to be found within the selvedges. Some biotites contain sagenitic textures (crystallographically oriented rutile needles), most of them exhibit fine-grained ilmenite or titanite along the borders (Figure 3.2). It seems, that sagenitic textures occur mostly in the "homogeneous neosome", but the reason why both rutile and ilmenite occur as an exsolution phase is still unclear. The limited amounts of Ca in these rocks might suggest titanite to be formed due to the later activity of a fluid, which can transport Ca ions of larger distances than solid state reactions.

Bigger grains of quartz, plagioclase as well as alkali feldspar often form aggregates, which exhibit irregular, roundish shapes. Due to the absence of the characteristic lamellae in plagioclase, feldspars are very hard to distinguish optically, which is why

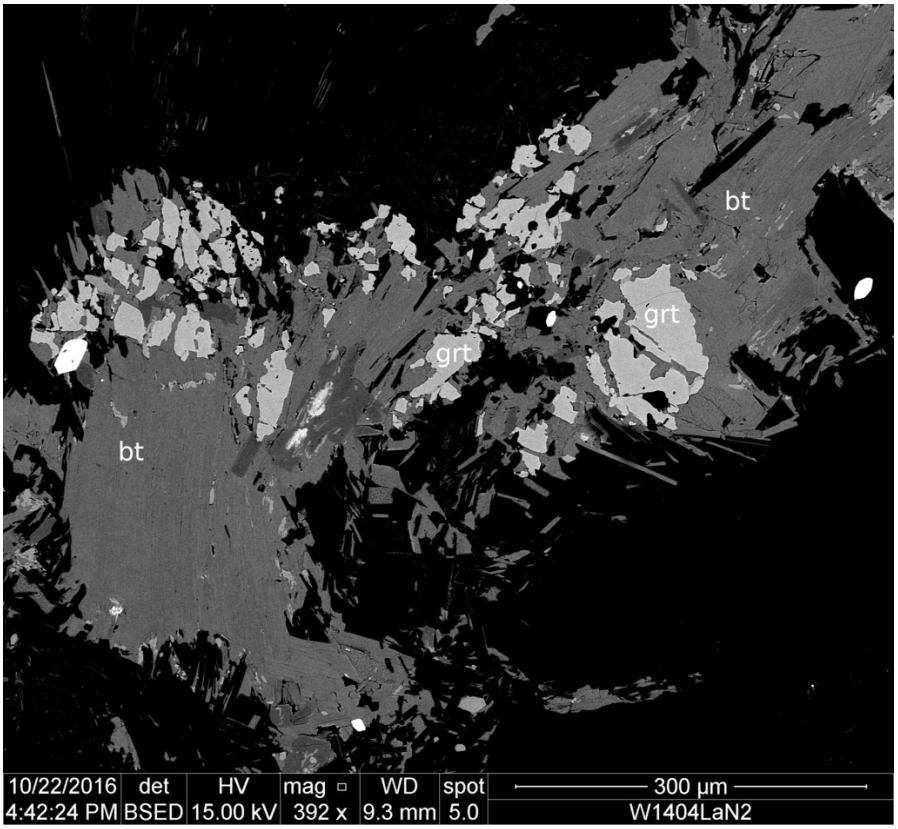

Figure 3.3.: SEM-image of garnet grains within biotite (Sample W1404LaN2)

the migmatite was also wrongly described as a tonalite (Schantl 1972; Schindlmayr 1999). Plagioclase is sometimes covered by needle-like zoisites. These never replace whole crystals, but only occur in patches.

The aforementioned bubbles are microscopically unorientated areas, with a high ratio of fine-grained matrix, which are surrounded by biotite-seams. These biotite-seams are sometimes part of the metamorphic layering within the schollen.

Garnet occurs mainly in reaction with biotite. The dissolution textures of biotite, combined with idiomorphic grain shapes of garnet shows the peritectic garnet to be the younger phase. Garnet is distributed over the whole migmatite-body (Klötzli-Chowanetz 2001), but is very unevenly distributed. Even in different thin-sections from one sample garnet does not necessarily appear in all of them. In the central area of the migmatite garnet is mostly idiomorphic.

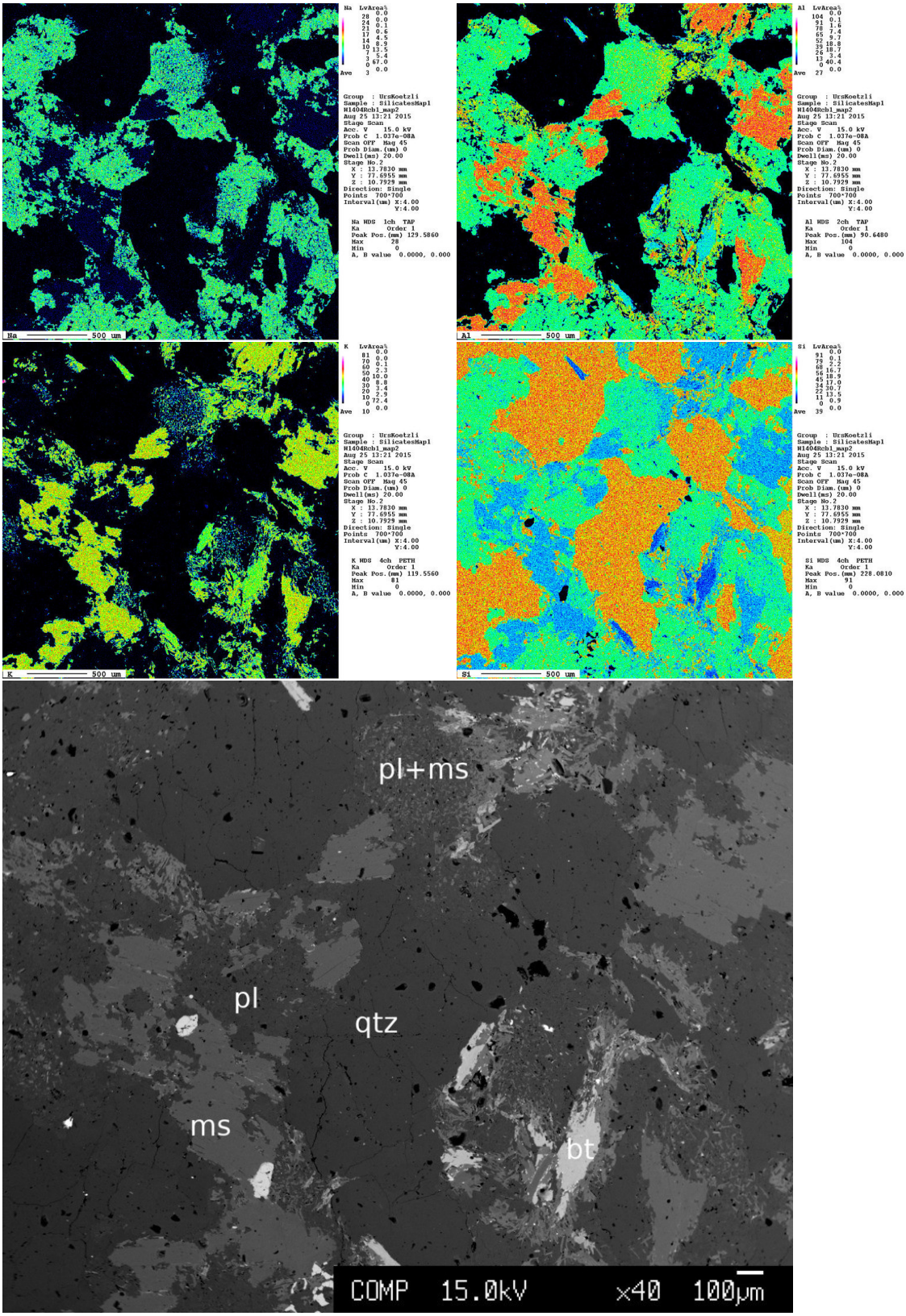

Figure 3.4.: EMPA maps for Na & Al, K & Si and corresponding BSE image of sample W1404Rcb, showing grains of quartz, white mica, biotite and fine-grained plagioclase (upper centre).

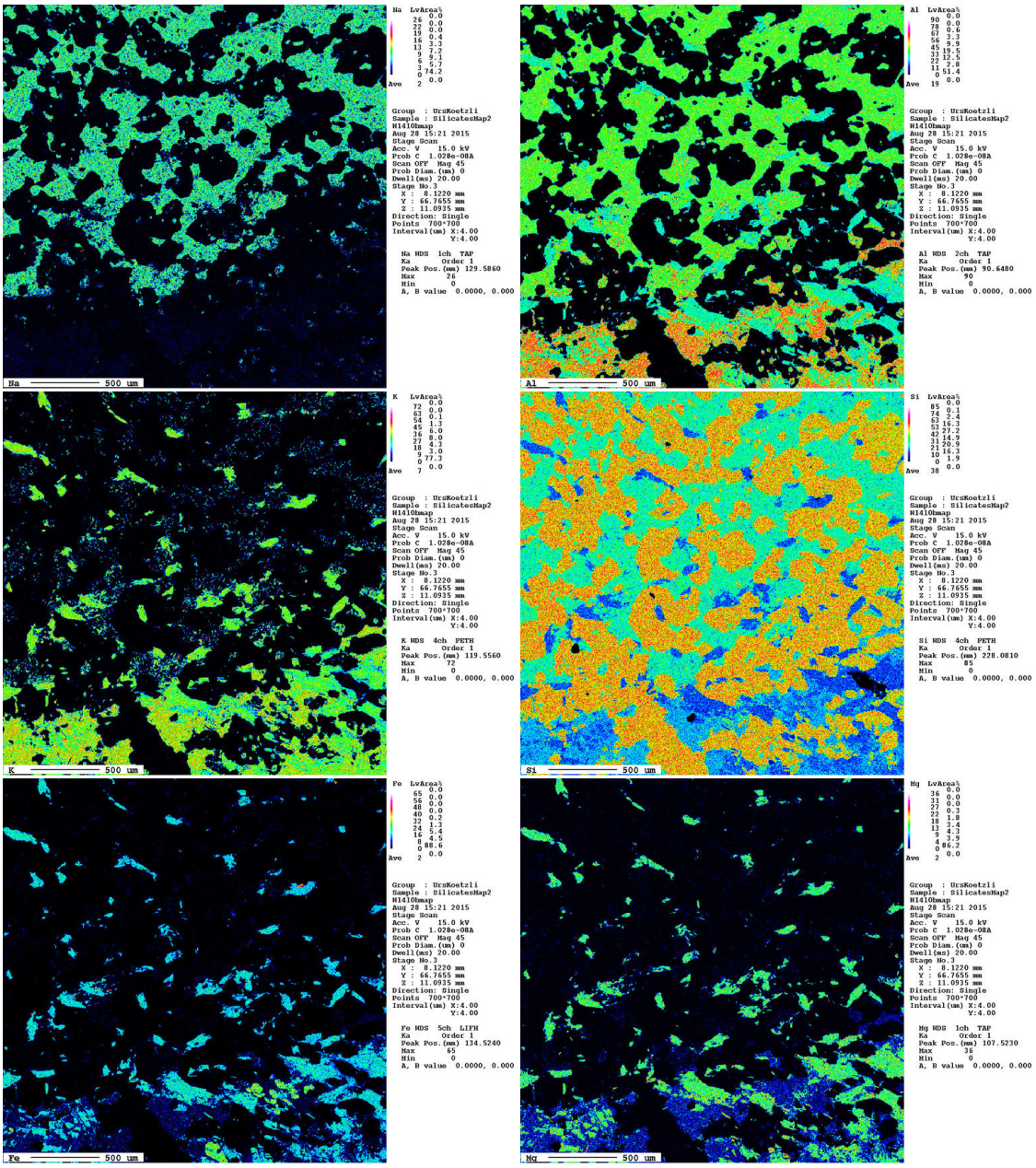

Figure 3.5.: EMPA maps for Na & Al, K & Si, Fe & Mg of sample W1410, showing a transition from a biotite-layer (lower half) to a more leucocratic area (upper half). For corresponding BSE image see figure 3.6

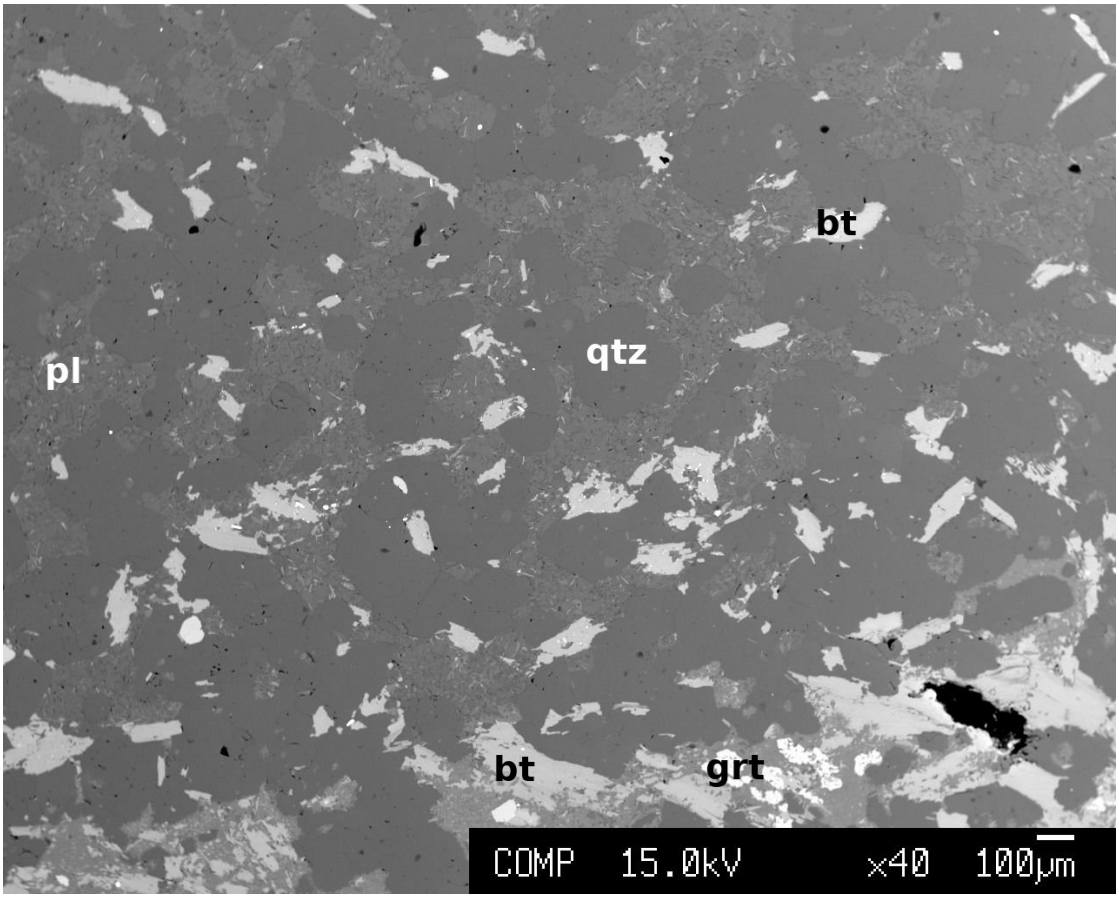

Figure 3.6.: BSE image of sample W1410, corresponding to figure 3.5. Transition from a bt-layer (lower half) to a more leucocratic area (upper half).

3.2. Mineral chemistry

Electron Microprobe Analyses (EMPA) were done to further investigate metamorphic reactions. Measurements where conducted on a JEOL JXA-8200 Microprobe at the Department for Applied Geosciences and Geophysics, Montanuniversität Leoben. Analyses of silicates were done at an accelerating voltage of 15kV, with a beam current of 10nA. Limits of detection are specified in Table B.1.

3.2.1. Feldspars

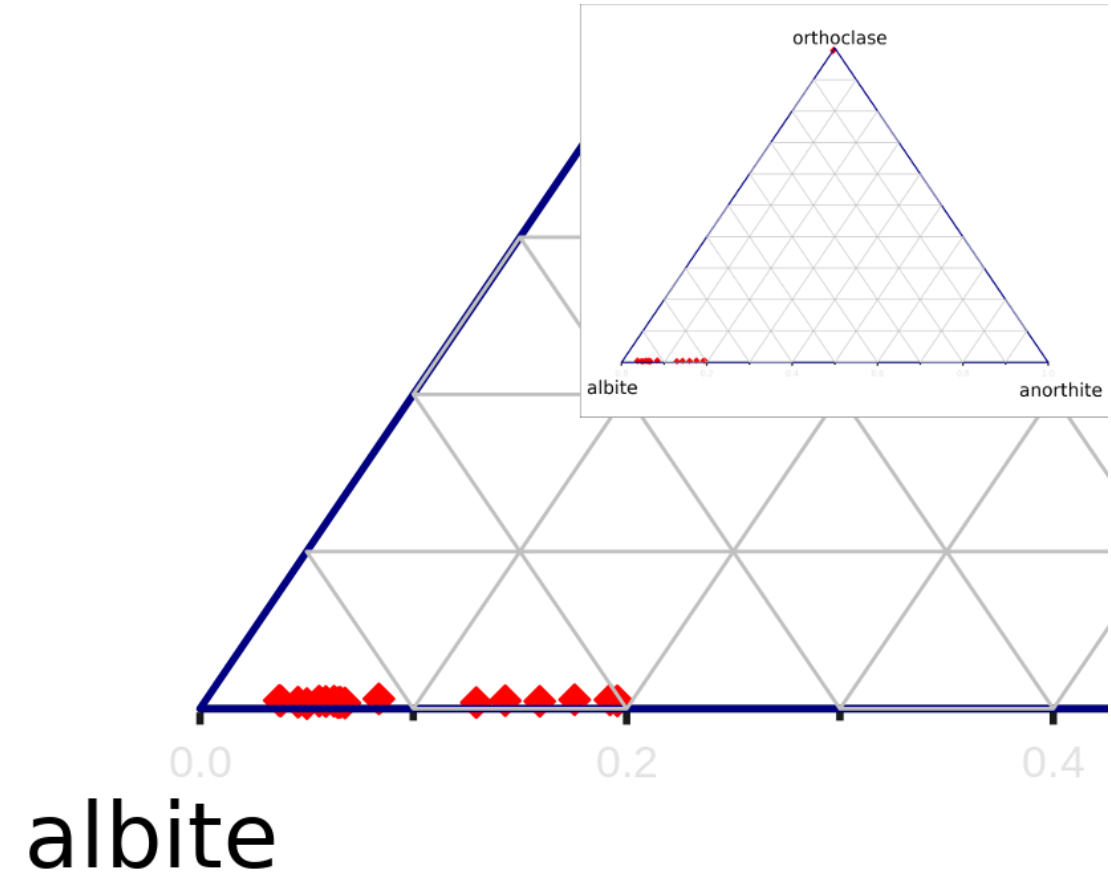

Figure 3.7.: Composition of feldspars, showing mostly albite and oligoclase, and 3 measurements of very pure orthoclase. Measurements are specified in Table B.2

Microprobe data show the majority of feldspars to be albite or oligoclase (Figure 3.7, Table B.2). These Na-rich plagioclases occur mostly in the fine-grained patches. Albite and oligoclase occur together in many occasions; there was no systematic difference in

distribution to be found in-between the two. Due to the relatively small sample size, these two clusters might represent a single cluster with an anorthite content of up to 20%. It should be mentioned, that Klötzli-Chowanetz (2001) also described separate clusters for albite and oligoclase. Orthoclase, however, was not found in these patches. In contrast to the very abundant plagioclase, alkali feldspar is relatively rare – only a single grain could be measured, which was independent from the granular plagioclase patches. Klötzli-Chowanetz (2001) describes orthoclase surrounded by fine-grained plagioclase in samples of homogeneous neosome, which could not be observed in these samples. As the samples investigated in this work represent either network or bubbles, this might be a subtle, but important difference.

3.2.2. White Mica

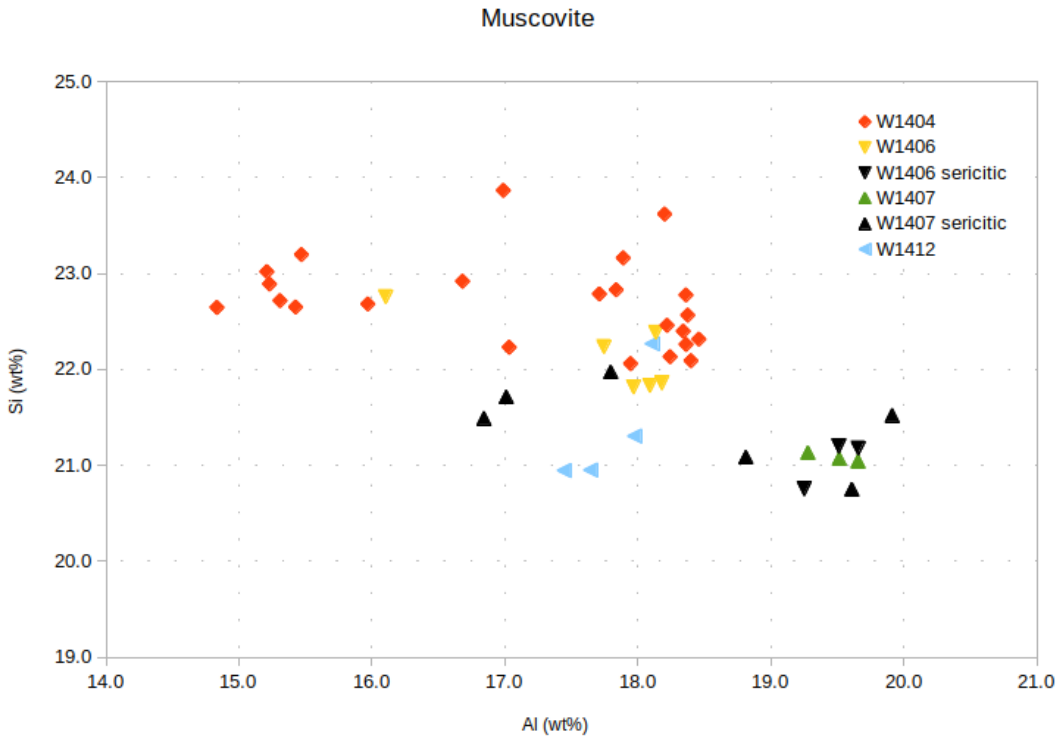

Figure 3.8.: Al and Si content of White Micas. Sericitic grains are represented by black symbols. Measurements are specified in B.3

Both populations of white mica, bigger grains ($> 100\mu$) and small (sericitic) grains ($< 20\mu$), were measured in the samples. While these are easily differentiated by their textures, there is no distinct, systematic variation in the chemical composition of the

two populations, instead a plot of Al and Si contents (Figure 3.8) show somewhat lower Si contents within sericites, but this is still within the cluster of bigger grains.

3.2.3. Biotite

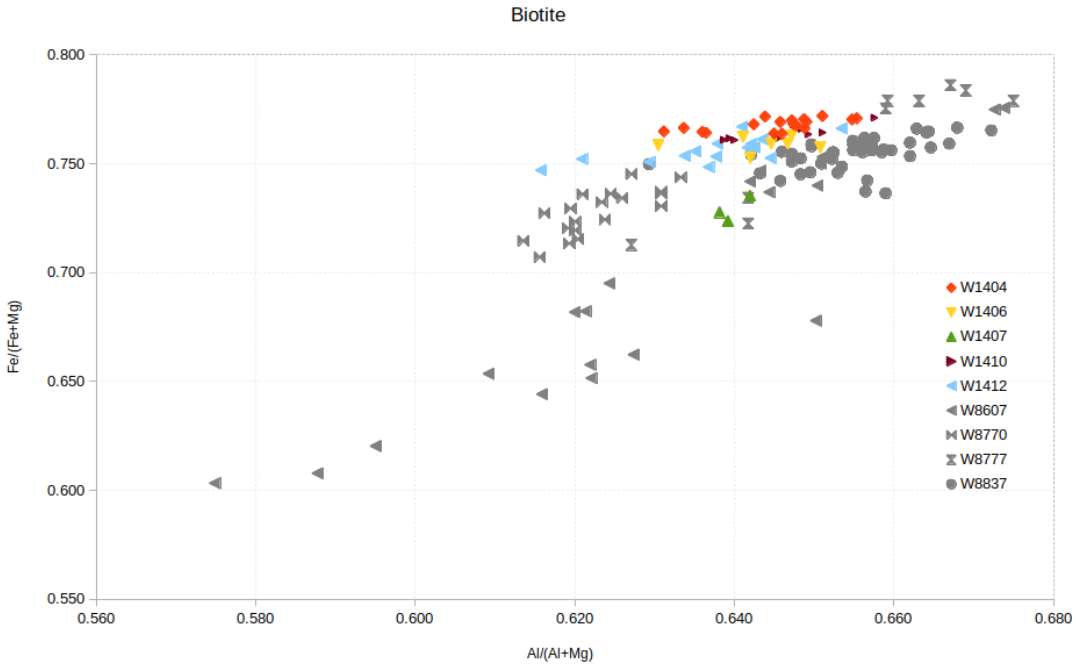

Figure 3.9.: Al/(Al+Mg) and Fe/(Fe+Mg) of biotite. Measurements are specified in B.4. Data from Klötzli-Chowanetz (2001) are plotted in grey.

Biotites show some minor variations, with crystals within coarse-grained quartz-"pinnite" patches (sample W1407) showing a lower $Fe/(Fe+Mg)$ number (Figure 3.9). However, compared to the data presented by Klötzli-Chowanetz (2001, plotted in grey), the composition appears on the higher end of the Fe/(Fe+Mg) spectrum, but still within the cluster.

Since Rb-Sr analyses of biotites result in mixed ages between $314 \pm 6Ma$ and $99 \pm 2Ma$ (Chowanetz 1990), attesting a post-anatectic overprint of at least 350 °C in the biotite isotope system (Dickin 2005), in the Variscan as well as at a later time, interpretation of biotite chemistry with regards to the anatexis seems futile.

3.2.4. Garnet

As mentioned beforehand, peritectic garnet occurs mostly in reaction with biotite. An appropriate reaction is given by Spear et al. (1999):

$$Biotite + Al_2SiO_5 + quartz = garnet + cordierite + K - feldspar + liquid$$

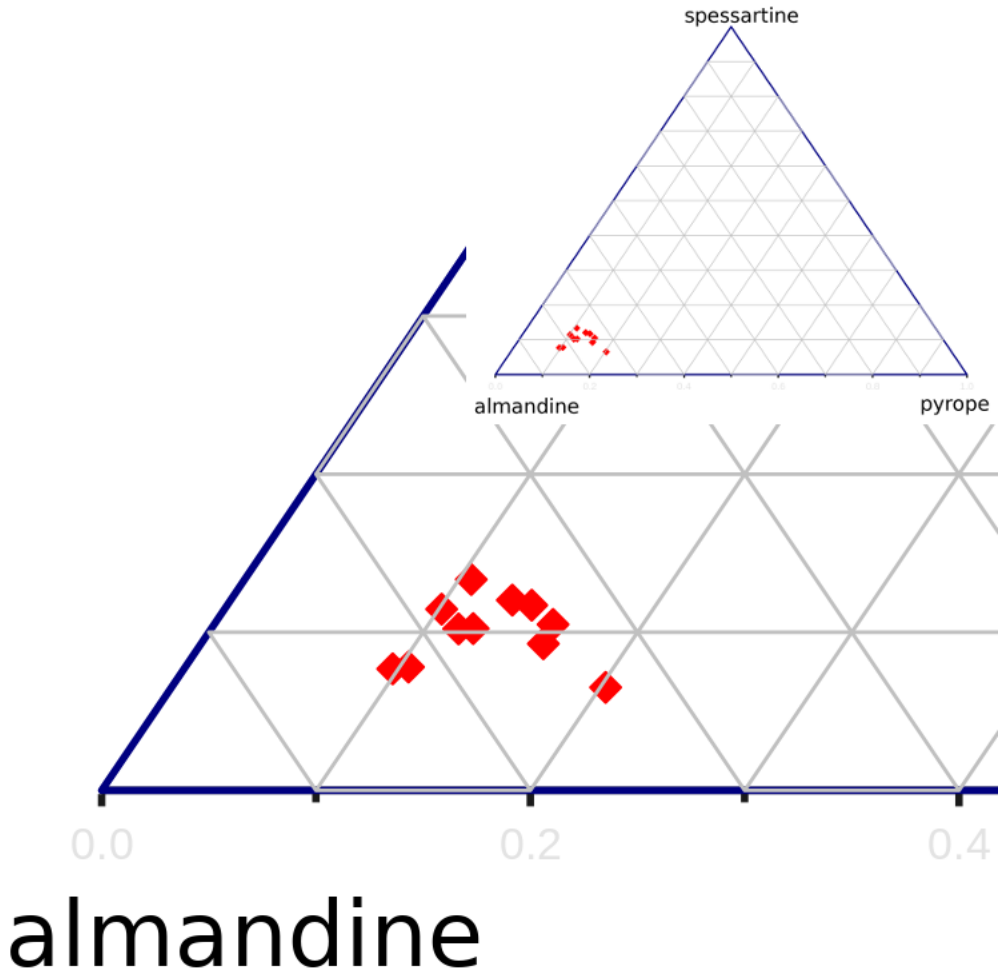

Figure 3.10.: Ternary composition of garnets from sample W1407. Measurements are specified in B.5

Chemically, no differentiation between idiomorphic and highly irregular garnet can be made – both consist mostly of almandine ($Fe_3Al_2Si_3O_{12}$), with only low fractions of pyrope ($Mg_3Al_2Si_3O_{12}$) and spessartine ($Mn_3Al_2Si_3O_{12}$)(Figure 3.10).

Within the green patches of so-called pinite, remnants of big peritectic garnet crystals were observed. These remnants are surrounded by chlorite and white mica and are strongly disintegrated into several parts, but can still be identified to be originating from a single large crystal. The remnants seem completely homogeneous, no zonation of any kind could be detected (Figure 3.12 and 3.11). Microprobe profiles through these garnets show no variation in chemistry. The absence of zonation might be explained by the reduction of grain-size, due to the breaking of these garnets, which increases the surface to volume ratio drastically, and in turn facilitates re-equilibration.

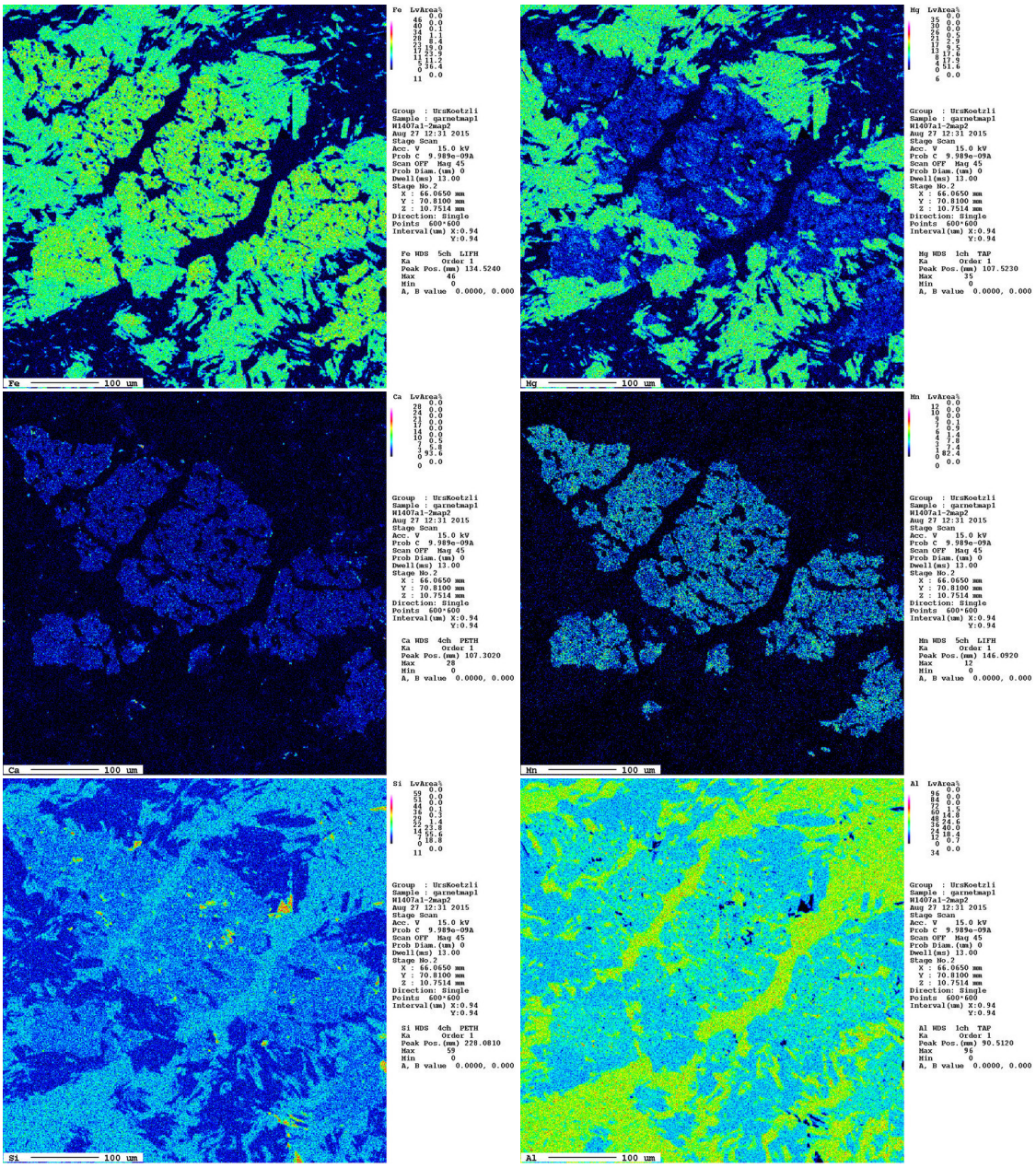

Figure 3.11.: Remnants of big Garnet surrounded by chlorite and white mica. EMPA maps for Fe & Mg, Mn & Ca, Al & Si. Sample W1407

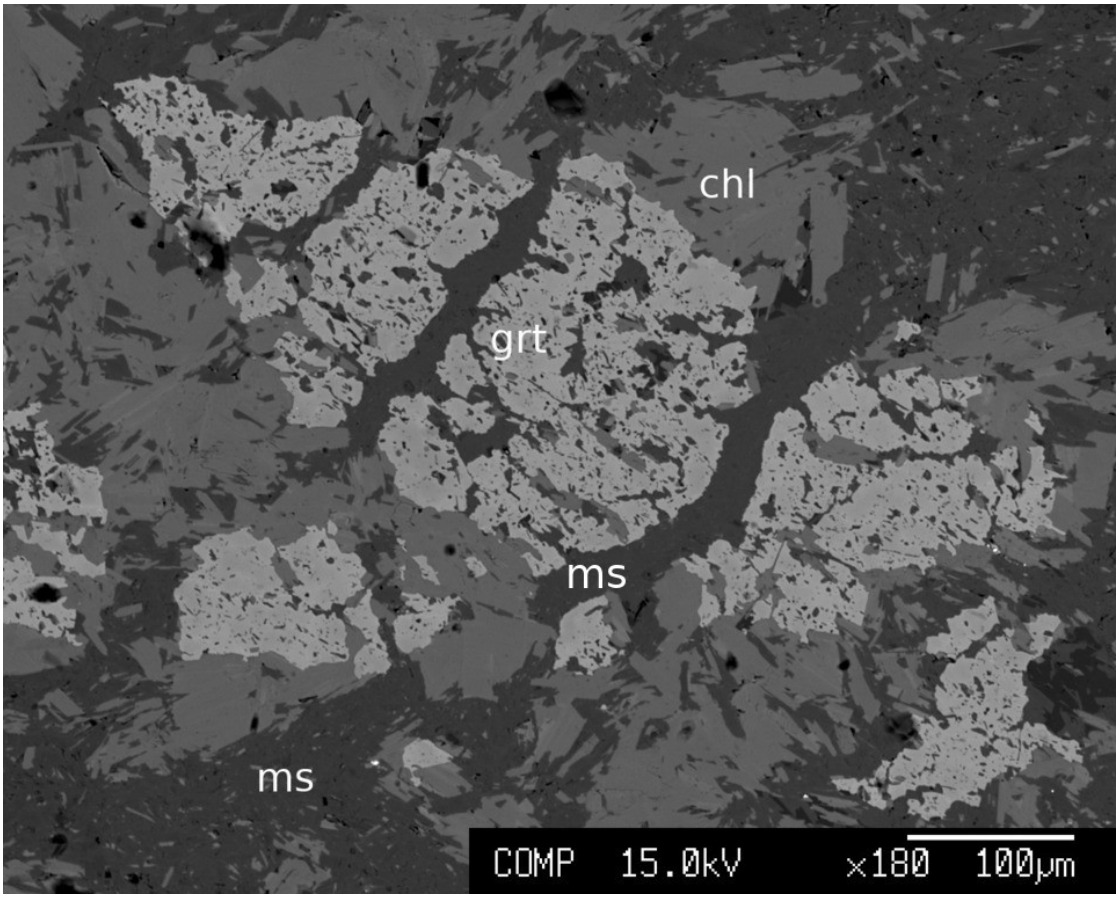

Figure 3.12.: Remnants of big Garnet surrounded by chlorite and white mica. BSE image of Sample W1407

3.2.5. Amphibole

Within a sample of calcsilicate, a single grain of actinolite was discovered (Table B.6, bottom line). Due to the extreme abundance of calcium in this lithology, these calcsilicates have very different mineralogical contents compared to the surrounding migmatite. Because it is only a single grain, its significance as evidence for metamorphic reactions is severely limited.

4. Geothermometry

Anatectic temperatures in the Winnebach migmatite are a subject of discussions in literature. Hoinkes (1973) states a maximum temperature of 685 °C, after conducting melting experiments under water-saturated conditions. Klötzli-Chowanetz (2001), however, considering Mg-rich garnet cores, claims temperatures of 700 °C and above, with the majority of garnets yielding lower temperatures, probably corresponding to post-anatectic reequilibration.

Many thermometers suffer resets in phases of metamorphism following the anatexis, thus making them unsuitable to determine anatectic temperatures. A promising approach for determining high temperatures might be the Ti-in-Zircon thermometer, which was subjected to testing for this case. This method holds the significant advantage that temperatures can be linked to geochronological data from the zircons.

4.1. Ti-in-Zircon Thermometry

The properties that make zircon so very well suited to the role of a geochronometer - namely chemical and physical robustness, and resistance to re-equilibration - also make it suitable as a geothermometer. Out of a variety of impurities within zircon (Hoskin and Schaltegger 2003), Watson et al. (2006) calibrated Ti content for use as a geothermometer. Experimental calibration was done on natural and synthetic samples, over a temperature range of approximately 600–1450 °C. Titanium content is described as being relatively independent of changes in pressure, but strongly dependent upon temperature, varying by over three orders of magnitude (Watson et al. 2006). While Titanium is present in lower concentrations than Hafnium or Yttrium, it is better suited to the role of a geothermometer because of better constraints on its activity in natural systems. As indicated by theoretical calculations, the dominant substitution seems to be $Ti^{4+} = Si^{4+}$, therefore, no charge-compensating substitution is needed (Harrison et al. 2005).

The calibration of Watson et al. (2006) defines a log-linear dependence of Ti content in Zircon as a reciprocal function of temperature:

$$\log(Ti_{zircon}) = (6.01 \pm 0.003) - \frac{5080 \pm 30}{T(K)}$$

This calibration was done for a rutile-saturated case, which constrains the activity of Ti (a_{TiO_2}) to one, and eliminates a correction for a possibly unknown activity. However, Ti can also be buffered in many other phases, which may offer similar constraints. For

instance, titanite or ilmenite also constrain a_{TiO_2} to high values, and can be regarded close to 1 in metapelites (Ghent and Stout 1984).

In addition, Zr content in Rutile can also be used as a thermometer, which works by the same principles as summarized above. There are three different calibrations for the Zr-in-Rutile thermometer, which come to slightly different results (Degeling 2002; Watson et al. 2006; Zack et al. 2004). Due to sparse occurrence of rutile in the investigated samples, only the Ti-in-Zircon thermometer was used.

4.2. Measurements

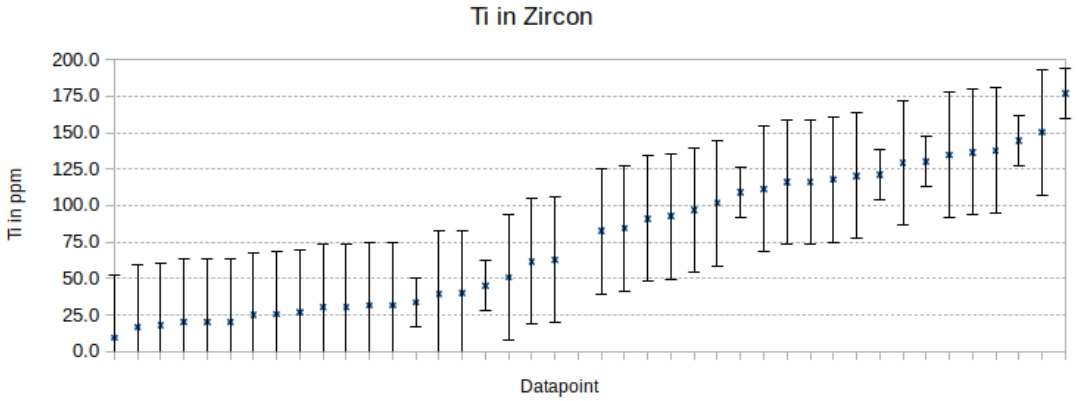

Figure 4.1.: Ti content in zircon, sorted in ascending order. Measurements are specified in C.3.

Measurements were done on a Cameca SX Five Electron Microprobe at the Department of Lithospheric Research, Vienna, mostly at 20kV and 30nA, another trial run was done at 15kV and 100nA for smaller zircons (for Limits of Detection see Table C.1 and C.2, respectively). The second run was an experiment to reduce the size of measurable zircons, to handle the generally very small zircons in the migmatite samples. For this reason, three spectrometers where used to measure Ti, resulting in lower detection limits as well as reduced spot size. The lower limits of detection are also reflected in lower errors in the calculation of temperature.

A limitation of microprobe analysis is the inability to measure low temperature, due to the incompatibility of Ti in zircon (Watson et al. 2006). As this thermometer was applied as a methodological test, this was an accepted drawback. Another limiting factor is the very small size of most zircon crystals in the samples, which excludes the possibility of measuring multiple points within one crystal. Thus, different crystal domains cannot be differentiated. In polymetamorphic rocks, with complex metamorphic histories, this is a severe disadvantage.

Adding to the errors of the calibration are analytical errors, which in this case are

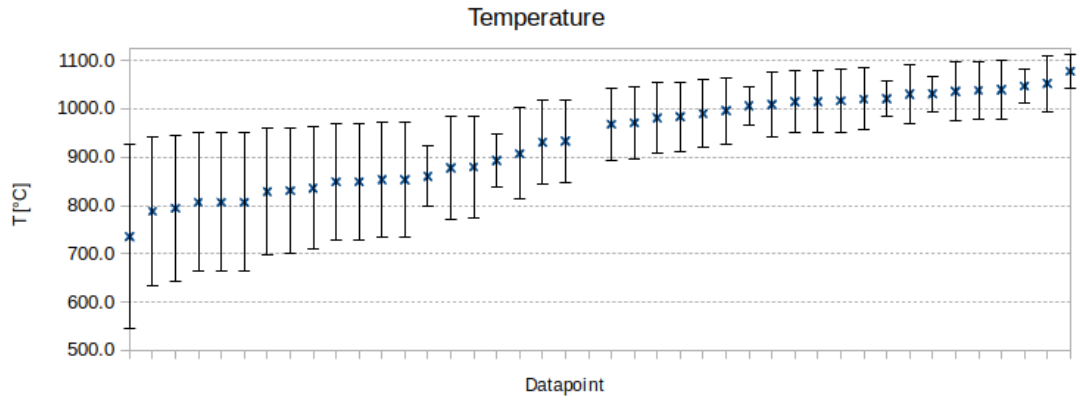

Figure 4.2.: Temperatures for zircons, sorted in ascending order. Measurements are specified in C.3. The blank space separates the higher plateau from the lower values.

represented as measured Ti-content ± detection limit. This conservative estimate was chosen because of the very low Ti-contents in this application, which approaches the limit of microprobe analytical work. This precaution can greatly inflate errors, especially for lower temperatures (Figure 4.1 and 4.2).

4.3. Results

Despite the stated analytical limitations, the data shows two plateaus of temperatures (Figure 4.2). The higher plateau is better defined, as the errors get smaller with higher temperatures, thanks to the logarithmic dependence on Ti content.

All of these measurements represent temperatures that are on the high end, or significantly above the range of anatectic temperature. Thus, these values correspond to pre-anatectic, inherited zircons. Because of the small grain size of the zircons, even small inherited cores with anatectic rims could result in an upward shift of seeming temperature.

A more in-depth analysis of the data, in conjunction with geochronological data is given in the Discussion (chapter 6).

4.4. Possible Improvements

As discussed, using a microprobe for Ti-in-Zircon thermometry presents some serious drawbacks. There are several options to mitigate these drawbacks to a certain degree: A well thought out measuring procedure (focused on Ti) helps to reduce detection limits, which is a big advantage in measuring lower temperatures. Synthetic zircons with fixed Ti contents at relevant concentrations (e.g. 0, 10, 50, 100 ppm) would facilitate

easier and more exact calibration, thus reducing detection limits as well as increasing precision. Despite these refinements, a microprobe is more suited to Ti-in-Zircon thermometry for high T applications, such as granulites, or for big zircon grains, without the need for measuring at high spatial resolution.

The most advantageous instrument would probably be an Ion Microprobe (IMP), which has the significant advantage of a very high spatial resolution due to a small spot size (down to approximatel 10μm). A high sensitivity facilitates measurements of lower temperatures. The downside of using an IMP is the lower availability of these machines, resulting in higher costs.

5. Geochronology

Because of its lack of post-anatectic deformation, the anatexis of the Winnebach migmatite was first thought to be Variscan (Hoinkes et al. 1972). Rb-Sr analyses on white mica from the undeformed central migmatite give a minimum cooling age of 461 $\pm$ 4 Ma, which is believed to represent cooling after the migmatization (Chowanetz 1991).

Complex Pb-loss in multiple stages is reported in data of conventional U-Pb zircon investigations, which plots in a discordia with intercepts of 670 Ma and 2275 Ma (Söllner and Hansen 1987). The lower intercept was interpreted as the age of the anatexis by Söllner and Hansen (1987).

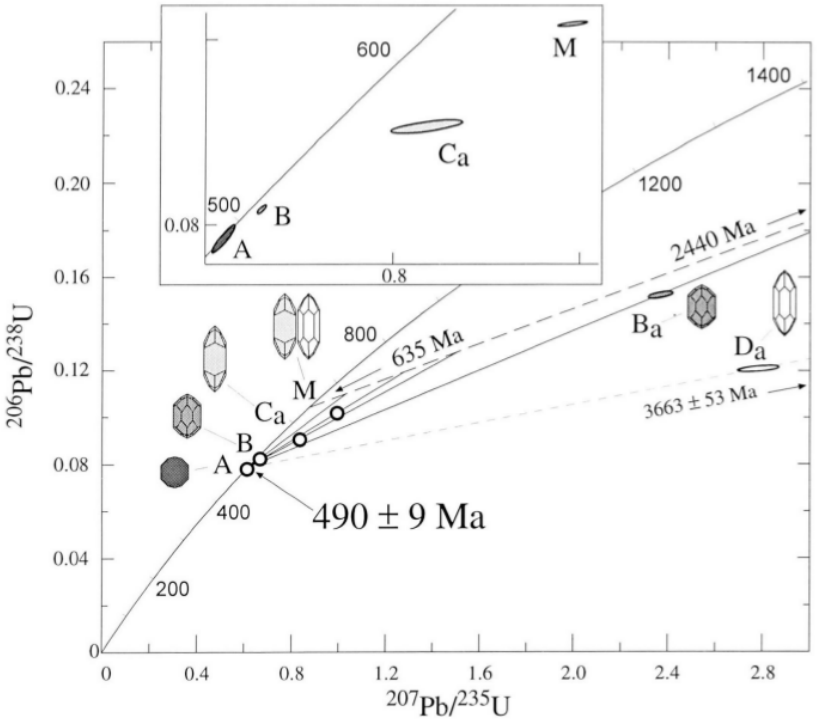

Figure 5.1.: Concordia diagram from Klötzli-Chowanetz et al. (1997): Population A gives a concordant age of 490$\pm$ 9 Ma, Populations B & C have been affected by lead loss. Population D appears to be of an older source than B & C. Fraction M is a mixture of C and D. The sub-index X_a refers to abraded fractions. The discordia from 635 Ma to 2440 Ma refers to single zircon evaporation results.

Zircon evaporation U/Pb analysis of zircons (method according to Kober (1986)) from the migmatite, as well as from the surrounding paragneisses revealed ages of 484 ± 6 Ma, approximately 560 Ma, as well as approximately 635 Ma within both the migmatite and the paragneiss (Klötzli-Chowanetz 2001; Klötzli-Chowanetz et al. 1997) (Figure 5.1). A "spheroidal, clear, inclusion free population of zircons" (Klötzli-Chowanetz et al. 1997) was found to be present only in the migmatite. This population yielded a conventional U-Pb age of 490 ± 9 Ma (Klötzli-Chowanetz 2001; Klötzli-Chowanetz et al. 1997) (Figure 5.2). Due to the absence of this population in the surrounding paragneisses, this age is attributed to the partial anatexis.

Thöny et al. (2008) reported U-Th-Pb electron microprobe ages of monazites within the leucosome of the Winnebach migmatite between 408 ± 46 Ma and 472 ± 36 Ma. The big errors associated with these ages, added to the vast spread of the data-points makes these results seem somewhat dubious as a basis for interpretation.

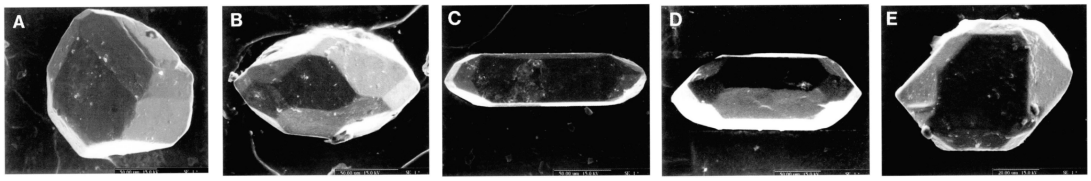

Figure 5.2.: Zircon populations measured by Klötzli-Chowanetz (2001) and Klötzli-Chowanetz et al. (1997): Population A occurs only in the migmatite, Populations B-E occur in the migmatite as well as the paragneiss

5.1. Measurements

To gain further insights into the complex history of the Winnebach migmatite, In-Situ analyses of zircons using the U-Pb system were conducted. For this purpose domains with high concentrations of zircons were cut out of samples using a micro-mill and embedded into resin. Measurements were done as single spot analyses on a SHRIMP (Sensitive High-Resolution Ion Microprobe) IIe-mc at the Polish Geological Institute in Warsaw.

Detailed imagery of zircons yielding the 610 ± 10 Ma concordia age is presented in Figure 5.3, in conjunction with data from thermometry. Three out of the four measurements are identical within errors, only Figure 5.3c represents an outlier, but even this lower temperature is partially negated by the huge error.

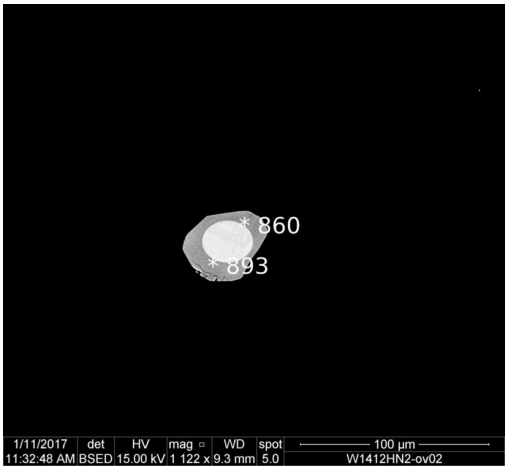

(a) Spot 1.1; W1412HN20v2_Zrk02: 860± 62 °C, 893 ± 54 °C

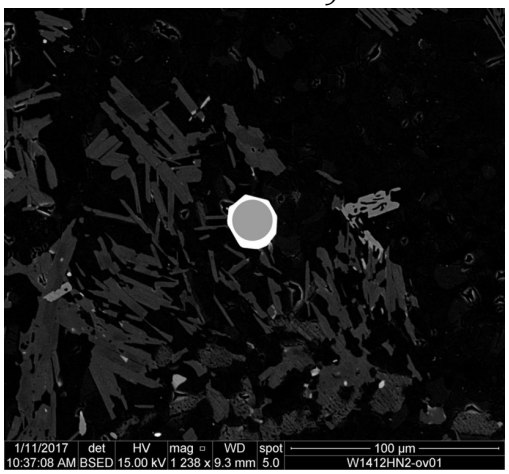

(b) Spot 2.2; W1412HN20v1_Zrk14: No thermometry measurements.

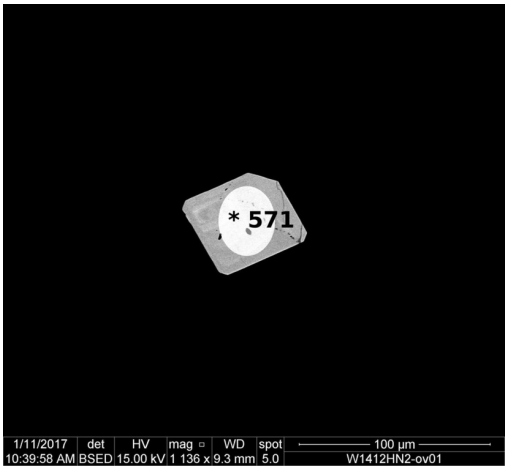

(c) Zircon 2.3; W1412HN20v1_Zrk15: 571 ± 334 °C

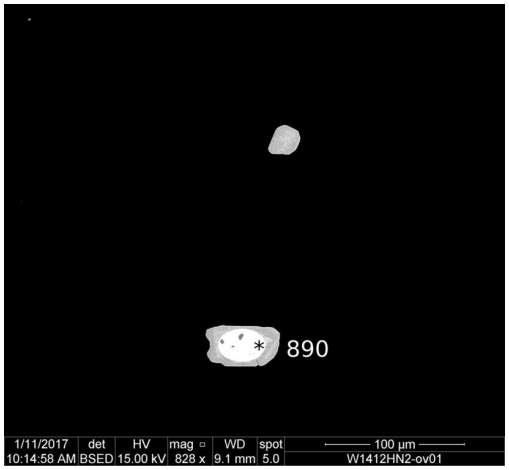

(d) Zircon 2.7; W1412HN20v2_Zrk03: 879±106 °C; 907± 95 °C

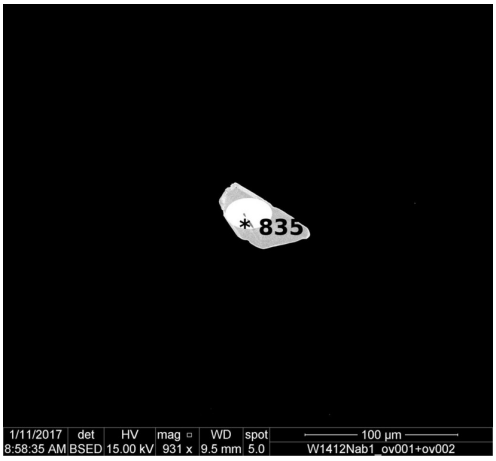

(e) Zircon 4.1; W1412Nab1_Zrk07: 835± 127 °C

Figure 5.3.: Detail images of zircons yielding a 610 ± 10 Ma concordia age. Spot measurements are indicated by ellipses, * denotes spots of thermometry, numbers represent calculated temperatures.

5.2. Results

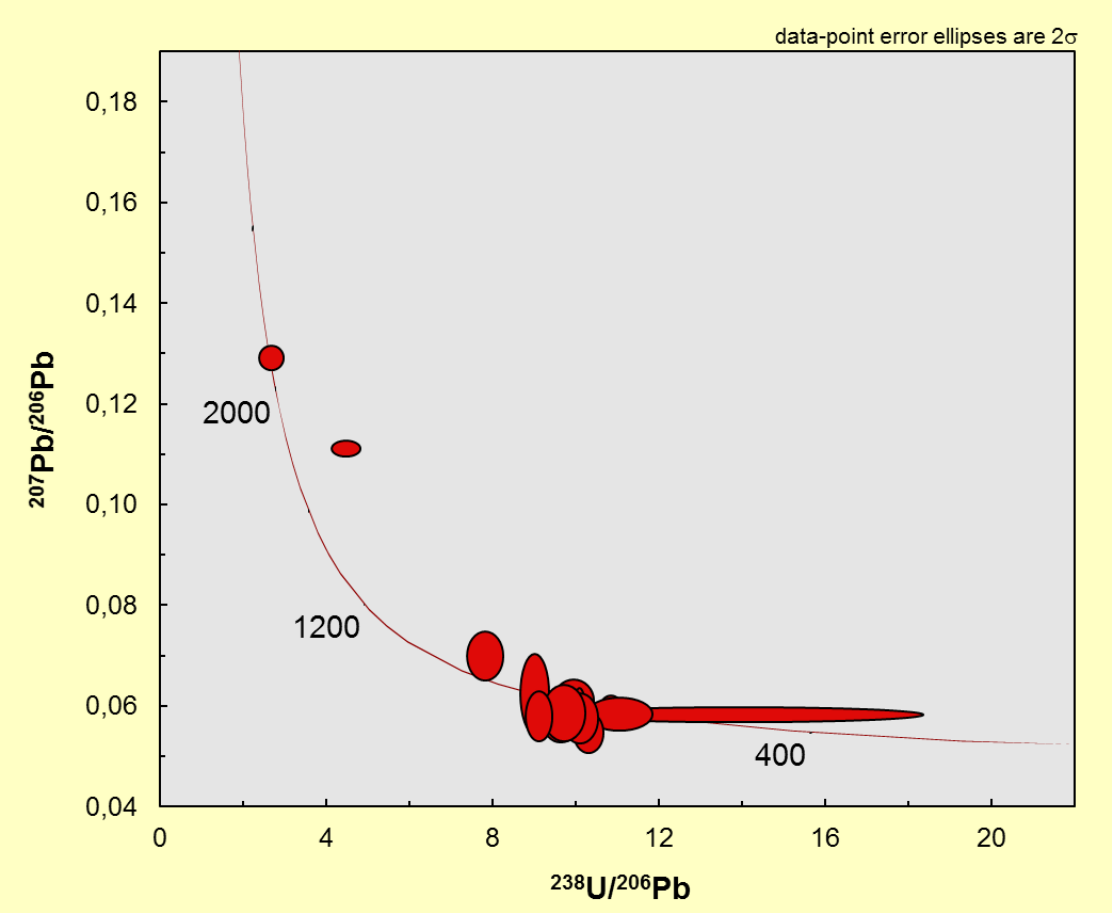

Figure 5.4.: Tera-Wasserburg Diagram of zircons from the central Winnebach migmatite, corrected for ^{204}Pb. Beside the big spread in ages, a distinct cluster is visible around 610 Ma. Data are specified in Table D.2

Ages were calculated from the raw data using the SQUID data reduction software (Ludwig 2009) in conjunction with the Isoplot tool-kit (Ludwig 2003). The detailed data are specified in Table D.2.

Plotted in a Tera-Wasserburg diagram the data shows a big spread in ages, with single spots over 2 Ga (Figure 5.4), which is in agreement with reports of inherited zircon cores in literature (Klötzli-Chowanetz 2001). Strong clustering is visible at approximately 610 Ma (Figure 5.5). A group of five spots overlapping within 2σ gives a concordia age of 610 ± 10 Ma. Notable is the relative concordance of most points. Single discordant spots suggest a possible discordia, however, because of the very small number of strongly discordant points no discordia was constructed.

Measurements 2.5 and 5.1 both showed significantly higher concentrations of ^{204}Pb

than the other measurements. Due to their big errors in $^{207}Pb/^{206}Pb$ after the correction for ^{204}Pb, both these measurements were discarded, and are not shown in the diagrams.

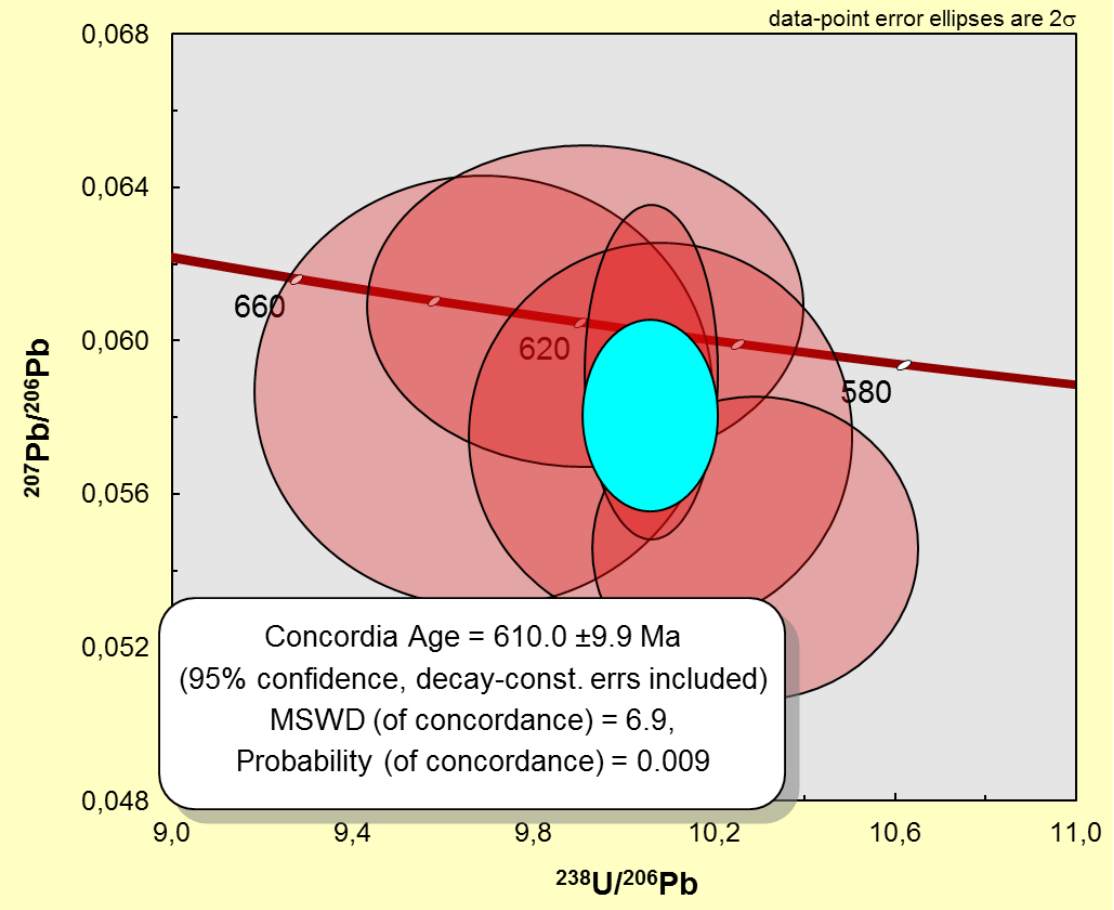

Figure 5.5.: Tera-Wasserburg Diagram of zircons from the central Winnebach migmatite, corrected for ^{204}Pb. Close-up of the cluster at 610 Ma.

It seems worth remarking that the age of 490 ± 9 Ma reported by Klötzli-Chowanetz (2001) and Klötzli-Chowanetz et al. (1997) could not be reproduced in these investigations. However, since this age was measured in separated zircons, out of which only a small fraction belonged to this fraction of spheroidal, multifaceted crystals, it seems likely that the small sample sizes of in-situ dating provide a very low probability of encountering these zircons. Thus, these new data are not regarded as a contradiction to the Cambro-Ordovician ages.

Instead, the concordia age of these investigations shows close correlation with ages from zircons within the Gaislehn granitic gneiss. This strongly foliated gneiss is directly adjacent to the Winnebach migmatite (See Introduction, Figure 1.2). In samples from this gneiss, Klötzli-Chowanetz (2001) describes rims around small inherited cores

(ages $>$ 2 Ga), which yield ages of 619 $\pm$ 28 Ma. These proterozoic rims are in turn overgrown by rims yielding an age of 475 $\pm$ 19 Ma (Figure 5.6).

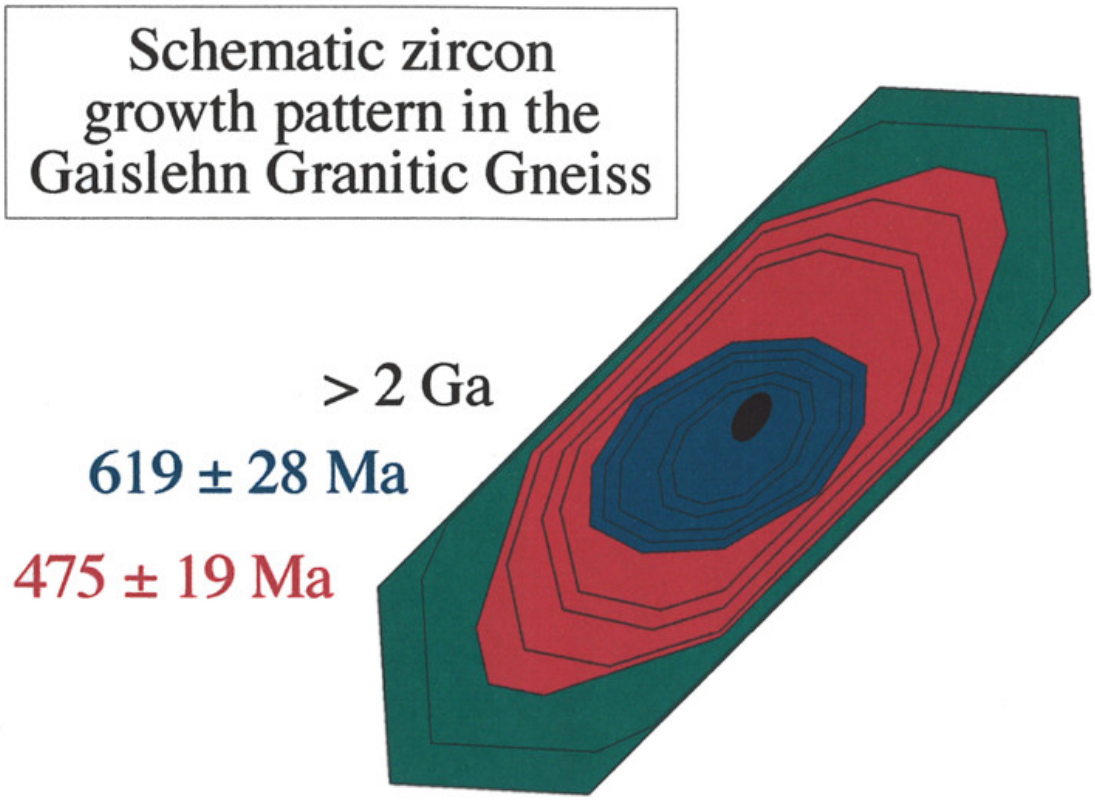

Figure 5.6.: Schematic zircon growth pattern in the Gaislehn granitic gneiss (Modified after Klötzli-Chowanetz (2001))

6. Discussion

6.1. PT estimates

Even though the Winnebach migmatite is undisturbed by post-anatectic deformation, post-anatectic metamorphism complicates interpretation of petrological data. Amphibolite-facies conditions of Variscan metamorphism reset most common geothermometers (Klötzli-Chowanetz 2001; Thöny et al. 2008).

Besides relying on thermometric data, PT conditions can be estimated by observing reaction textures related to the anatexis. For this purpose, a petrogenetic grid calculated by Spear et al. (1999) is applied (Figure 6.1).

Even though this grid is calculated for metapelites, it is employed as a first-order approximation for these meta-greywacke rocks. This model assumes dry conditions, where the only water available for melting reactions comes from dehydration of hydrous minerals. This assumption of a dry system is supported by geochronological evidence for pre-anatectic metamorphism (Klötzli-Chowanetz et al. 1997; Söllner and Hansen 1987).

Dissolution textures of muscovites are interpreted as evidence for dehydration melting. On a prograde path below invariant point 1 (IP1, Figure 6.1), dehydration of muscovite would produce alkali feldspar, which would manifest as porphyroblasts or finely dispersed grains of alkali feldspar (reaction [1]). Vice versa, a retrograde path below IP1 would produce fine-grained alkali feldspar, instead of the fine-grained, dispersed muscovite that is present in the investigated samples. Thus, reaction [2] or [3] can be assigned to the breakdown of white mica.

Similarly, the dehydration melting of biotite is represented by reaction [8] or [9]. However, since no orthopyroxene is present in the samples, this reaction can be used to estimate a maximum temperature. This reasoning yields a rough temperature estimate of 700 – 800 °C, and a pressure estimate of at least 4 kbar. It bears mentioning that pre-Variscan thermobarometry of the Winnebach migmatite is still a topic of discussion within literature. Hoinkes (1973) states a minimum temperature of 685 °C, obtained by melting experiments.

Klötzli-Chowanetz (2001) states pressures of $\geq$ 8 kbar, on account of two different generations of kyanite, one of which is attributed to the anatexis.

Thöny et al. (2008) assume garnet and kyanite to be of Variscan origin, and calculate a pressure estimate of $<$ 2.8 kbar.

Pressures this low would mean almost contact-metamorphic conditions, which seems like an unecessarily complicated explanation in rocks with a polymetamorphic history, as it requires the assumption of a previous exhumation to depth smaller than 10 km.

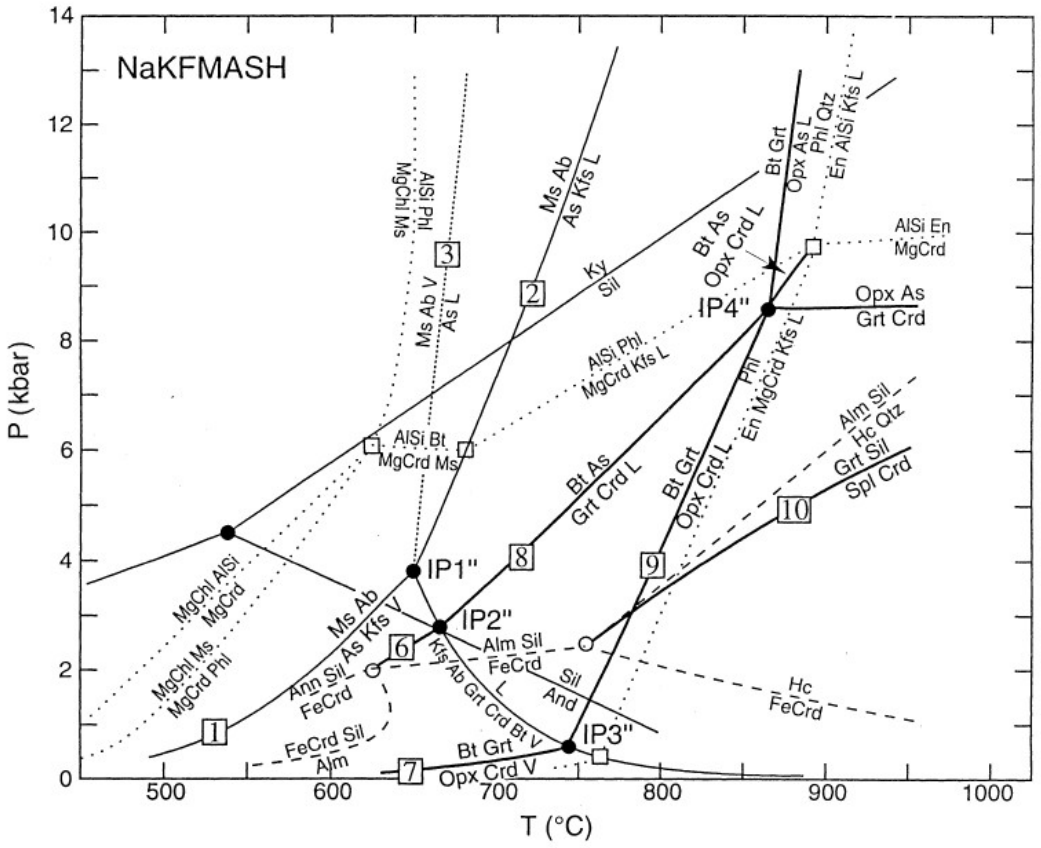

Figure 6.1.: Petrogenetic Grid by Spear et al. (1999): Pressure temperature diagram of selected melting and dehydration reactions within the NaKFMASH system. Dashed lines: KFASH system; dotted lines: KMASH system; finely dotted lines: pelite vapour-saturated melting reaction.

In conjunction with the relative scarcity of K-feldspar compared to muscovite in the investigated samples, this makes the pressure estimate of Klötzli-Chowanetz (2001) appear the geologically more realistic one. Also, at lower pressures, the expected melt composition would move towards higher contents of quartz and orthoclase, respectively (Johannes and Holtz 1996). This shift in melt-composition could provide a way to settle the debate about pressure.

6.2. Lithologies and Textures

The process of partial anatexis gives rise to new lithologies. The diversity in observable textures can be explained as different stages of melting, more specifically as different

amounts of melt produced. Different melting rates can most likely be attributed to differences in chemistry within the protolith. The amount of eutectic melt produced is inversely proportional to the anorthite-content within the paragneiss (Hoinkes et al. 1972). With rising temperatures and thus growing amounts of melt, early intergranular melts join up to become bubbles, which in turn can empty into existing pathways, or grow into networks of their own. With increasing amounts of melt, fractionation of the bt-pl gneisses appears, and melts are progressively separated from solid phases. Schollen of bt-schist can be regarded as end-members of this process, collecting remaining quartz and plagioclase in addition to the biotite. To incorporate the model of partial melting by Kriegsman (2001) lets a back-reaction seem a likely additional reason. The occurrence of biotite selvedges along melt-channels without flow textures can be interpreted in terms of a back-reaction, which further intensifies the appearance of these dark bands. Kriegsman (2001) regards this retrograde back-reaction as the driving force in the formation of melanosomes.

Flow structures around schollen suspended within the homogeneous neosome as well as melt channels cutting through schollen indicate a certain degree mobility of the melt. Thus, the textures of the winnebach migmatite represent a record of beginning melt-extraction. Studies of thickness and spatial distribution of leucosomes in migmatic units of the Fosdick migmatite-granite complex (West Antarctica) demonstrate scale-invariant spatial distributions. However, differences in the distribution were found, depending on whether the protolith was a paragneiss or an orthogneiss. This is attributed to the different "inherited compositional layering"(Yakymchuk et al. 2013). These results support the notion that melt-extraction is a self-organized process (Yakymchuk et al. 2013). This is consistent with field observations of melt channels of strongly varying sizes. The beginning melt-extraction and the separation from the restite means that these melts cannot be described as in-situ. (The distance the melt moves away from the corresponding restite can not be quantified.) The term in-situ, however, can at the most be applied to non-segregated melts within schollen, which would be classified as mesosome.

The so called homogeneous neosome, containing biotite, must also be classified as a mesosome. But instead of schollen, where the melt remained in-situ within the pre-anatectic layering, the progressive melting resulted in a dissipation of previous textures, producing a wholly unoriented texture. Thus, the term homogeneous neosome (chosen for clarity within the context of literature, as it was first described using this name by Hoinkes et al. (1972)), is somewhat misleading, as the amount of melt was probably rather small, and by no means the majority of the volume. However, the melts were not removed from the restite.

The K-feldspar described by Klötzli-Chowanetz (2001) within the granulated feldspar of the HN, which is totally absent in samples of melt channels and bubbles, might be an indicator for non-segregated melts.

6.3. Thermochronology

Since the thermometry was only able to measure Ti-contents representative of high temperature, application of the data is somewhat limited. While anatectic temperatures of approximately 900 °C would be in disagreement with every interpretation found in literature, these temperatures seem reasonable in light of the fact that geochronology only shows pre-anatectic ages. Most likely these temperatures represent magmatic temperatures recorded in the old zircon cores.

To produce thermometric data usable for PT-estimation of anatectic conditions, a significant lowering of detection limits is required. This could be facilitated by using an IMP as measuring instrument. Ti-in-Zircon thermometry, especially when combined with studies of zircon typology could possibly be a way of pinpointing anatectic temperatures. A detailed investigation into the Ti-content of 'Zircon Population A' reported by (Klötzli-Chowanetz 2001) could be a promising approach.

6.4. Concordia ages

The concordia age of 610 Ma is further evidence for pre-anatectic temperature peaks (Figure 5.5). The occurrence of the same age in the adjacent Gaislehn granite gneiss suggests affiliation. In fact, the geochronological data from the Gaislehn can easily be matched to the Winnebach's. In the Gaislehn, a Proterozoic core (age $>$ 2 Ga) is overgrown by a short-prismatic zircon rim with an age of 619$\pm$ 28 Ma (Figure 5.6). This is identical within error with above-mentioned concordia age. A second zircon rim (elongate prism, dipyramidal) from the Gaislehn zircons yields an age of 475$\pm$ 19 Ma, which in turn might be correlated to the 490$\pm$ 9 Ma age of the spheroidal Winnebach zircon population. It has to be noted, that the latter one is a concordia age, while the corresponding age of the Gaislehn is a discordia age calculated for recent lead loss. Thus, the age disparity – even though overlapping within error – is relativised and the Gaislehn age can be attributed to the (better defined) Winnebach age. In the Gaislehn, an outermost, thin rim is present for which no geochronological data exists. (Klötzli-Chowanetz 2001)

This correlation suggests a common metamorphic evolution of the adjacent units. The ages of 610 $\pm$ 10 Ma, and 619$\pm$ 28 Ma, respectively demonstrate a late-Proterozoic thermal peak. Due to the shape of the corresponding zircon rim (Harley et al. 2007; Klötzli-Chowanetz 2001; Pupin 1980) in the Gaislehn granite gneiss, this thermal event is interpreted as the intrusion and subsequent cooling of the Gaislehn granite.

The granite and the paragneiss then experience a further stage of metamorphism (475$\pm$ 19 Ma, and 490$\pm$ 9 Ma, respectively), which leads to anatexis in the paragneiss, and possibly in the granite. The long pyramidal shape of the zircon rim in the Gaislehn is indicative of fluid-saturated metamorphism (Klötzli-Chowanetz 2001). Furthermore, similar microscopic textures are reported for the granite gneiss, including zoisite growth on plagioclase, and lenticular pseudomorphs of sericite after alkali feldspar (Bidner 1989; Klötzli-Chowanetz 2001). Corresponding ages are also evident

in the non-anatectic paragneiss (Klötzli-Chowanetz 2001), as well as in the Ordovician magmatism in the central and western Ötztal Complex (Bernhard et al. 1996; Schmidt et al. 1967). Th/U ratios of the concordant zircons, and zircons from the Gaislehn gran-

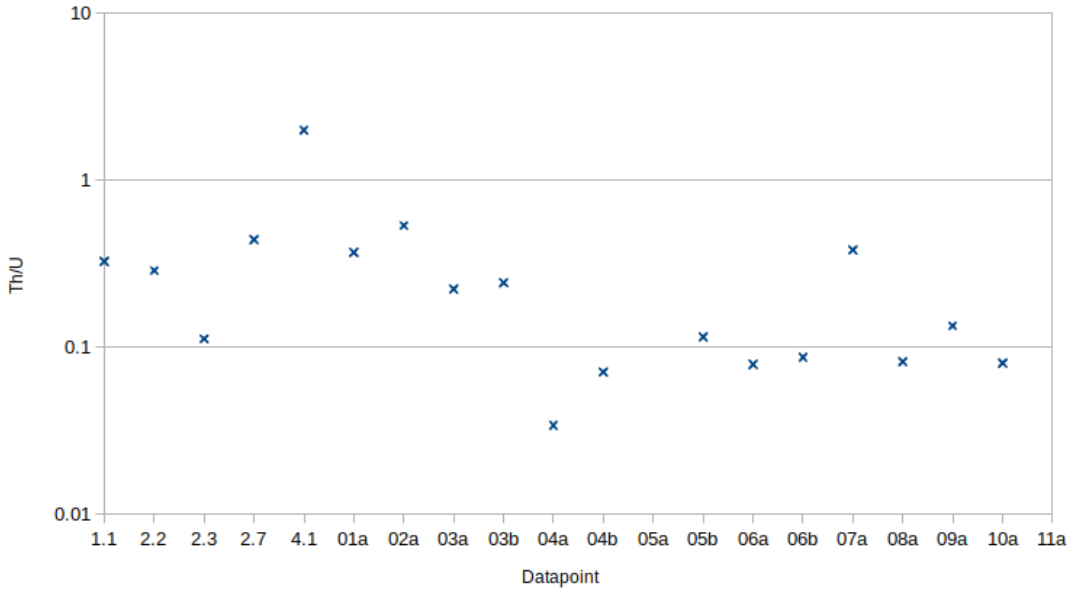

Figure 6.2.: Logarithmic plot of Th/U ratios of zircons from the Gaislehn granitic gneiss and zircons from the Winnebach migmatite (first five spots) yielding the corresponding concordia-age. Data specified in Table D.1.

ite gneiss were investigated, in the search of further similarities apart from age. This ratio is commonly used to distinguish between magmatic and metamorphic zircons, with magmatic zircons showing a ratio of > 0.1 (Rubatto 2002; Rubatto and Gebauer 2000). Th/U ratios in the Gaislehn zircons show a spread from 0.03 to 0.53, while the Winnebach zircons give ratios between 0.11 and 0.44, with one extreme outlier at 1.99 (Figure 6.2). According to the aforementioned distinction, all the Winnebach zircons would be classified as magmatic, while the Gaislehn zircons exhibit both magmatic and metamorphic signatures. However, regarding the very small number of points, reliable interpretation of this data might not be possible. Moreover, Möller et al. (2003) call the practice of this Th/U based distinction into question, and point out counter-examples where distinction between magmatic and metamorphic zircon using this method is not possible.

Slightly younger ages down to 430 Ma are also reported from intrusives in the central ÖC (**Kloetzli2008**; Thöni 1999), from the Klopaier migmatite (Klötzli-Chowanetz 2001) and granitic dikes emplaced discordantly in the Winnebach area (Söllner and Hansen 1987, 444$\pm$ 4 Ma). Monazites of the migmatites in the ÖC, dated by electron microprobe, yielded mainly Ordovician-Silurian ages (Thöny et al. 2008, 408$\pm$ 46 Ma to 472$\pm$ 36 Ma for the Winnebach migmatite, 409 $\pm$ 50 Ma to 457 $\pm$ 42 Ma for the Ver-

peil migmatite, 431± 37 Ma to 472 ± 31 Ma for the Klopaier migmatite). These ages were reported as belonging to the anatexis, but taking the big spread into account, in addition to the already big errors, interpretation of these ages as one metamorphic event seems somewhat daring. Due to the presence of Variscan monazites in the same samples, the possibility of mixing ages must be carefully ruled out for a meaningful interpretation. However, the quantity of Ordovician-Silurian ages in the ÖC cannot be ignored, even if the exact nature of the event is unknown.

The outermost zircon rim distinguished by Klötzli-Chowanetz (2001) in the Gaislehn granite gneiss may correspond to Variscan metamorphism, which might also be the cause of deformation of the Gaislehn. Although distinguishable by crystal habit, this rim was too narrow to date. The only marginally deformed Winnebach migmatite shows no post-anatectic growth of zircons, but Variscan Rb-Sr ages can be obtained from white mica (Chowanetz 1991).

The presence of "Gaislehn ages" within the migmatite necessitates some further explanations. Two different mechanisms for the emplacement of "Gaislehn zircons" into the Winnebach paragneiss (not yet migmatic) seem conceivable: Firstly, the development of apophyses from the plutonite into the surrounding meta-sediment: This process would deposit material within the paragneiss, which might further account for the great chemical and textural diversity of lithologies in the migmatite. Secondly, an assimilation of the migmatite and the granite by the jointly experienced anatectic conditions. This mechanism would assume the transport of melt between the two bodies, moving pre-anatectic zircons from the Gaislehn into the Winnebach. Even though 4 of the concordia-spots are found in the network of neosome, one of them is located in the melt-bubbles, which makes this scenario seem less likely. Also, the distance of more than one kilometre from the sample location to the lithological border of the migmatite with the Gaislehn would require long-range transport of melts. The lithological border may however have been blurred by Variscan metamorphism, and the resulting deformation. A growth of zircon based on contact metamorphism alone also seems unlikely because of these field relations.

7. Conclusion

These investigations demonstrate the difficulties inherent in deciphering the history of polymetamorphic rocks. Due to the re-equilibration in post-anatectic metamorphism, anatectic conditions are badly constrained. Ti-in-Zircon thermometry, especially combined with U-Pb dating of zircons is believed to provide new possibilities in this field. The thermometric methodology is shown to be applicable, given a lower detection limit for Ti. An optimal solution would be to include measurements of Ti with U-Pb measurements on an IMP. Also, a specific investigation of the Ti-content in the zircons yielding anatectic ages is highly suggested.

The geochronological data attests a correlation between the Gaislehn granite gneiss and the Winnebach migmatite. The late-proterozoic age is interpreted as the intrusion of the Gaislehn granite. Further investigations into the trace elements within these zircons might help to shed some more light on this topic.

The different lithologies within the migmatite can be ascribed to differences in chemistry within the protolith. The biotite-plagioclase gneiss begins partial melting in suitable (Ca-poor) domaines. The products of this process, restite and melt, can now either be separated, or stay next to each other. The reason for these two opposed behaviours is unclear, most probably this is a result of subtle differences in texture and the amount of melt produced. On the one hand, if the melt remains unsegregated from the restite, a partial back reaction leads to the formation of the mesosome. In the case of the Winnebach this is represented bt-pl schollen, as well as the so called homogeneous neosome, even though the pre-anatectic texture of the HN was dissipated (Figure 7.1, left hand side).

On the other hand, if the melt gets segregated from its corresponding restite, it can have a partial back reaction with the adjacent restite at the point of cooling below a certain temperature. This leads to the formation of a leucosome and a melanosome. In this case, this corresponds to small haplogranitic melt-channels lined with biotite, and biotite schists with adjacent areas of coarse grained quartz and feldspar (Figure 7.1, right hand side).

K-feldspar within pockets of granulated plagioclase is described in the homogeneous neosome, but was not found in samples of melt channels, bubbles and network. Systematic investigations into the occurence of pre-anatectic feldspar might prove this to be a valuable indicator of unsegregated melts.

Even though there is no geochronological evidence for multiple melting events as of now, the application of the migmatite model by Kriegsman (2001) helps to shed some light on the plethora of lithologies and textures observable in the Winnebach migmatite. Methodological advances in In-situ dating might provide the possibility of dating zircons in higher spatial resolution, thus allowing the decoding of zircon rims.

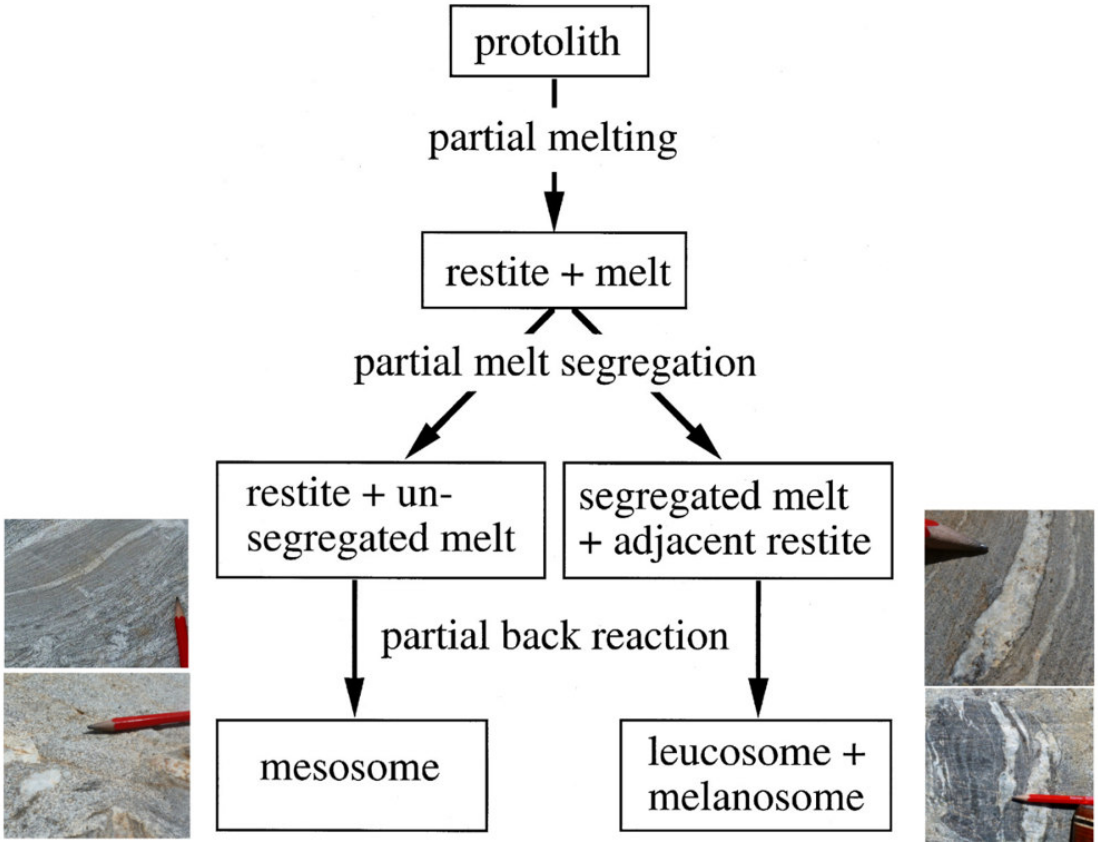

Figure 7.1.: Flowchart of Kriegsman's model of migmatite evolution, modified after Kriegsman (2001). Images represent end products of migmatization. The left hand side show bt-pl scholle (top) and homogeneous neosome on the bottom, as examples for the mesosome.
The right hand side shows a small melt channel of haplogranitic composition, with a biotite selvedge on the top, the bottom shows a bt-schist scholle, with coarse grained layers of quartz and feldspar.

Bibliography

Bernhard, F., U. Klötzli, and M. Thöni (1996). "Age, origin and geodynamic significance of a polymetamorphic felsic intrusion in the Ötztal crystalline basement". In: *Austria. Miner. Pet.* 58, pp. 171–196.

Bernhard, F. (1994). "Zur magmatischen und metamorphen Entwicklung im westlichen Ötztal-Stubai Kristallin; (Bereich Feichten - Verpeil, mittleres Kaunertal)". Diplomarbeit. Universität Graz, p. 314.

Bidner, T. (1989). "Zur Petrographie des Granitgneises vom Gaislehnkogel (Oberes Sulztal)". Diplomarbeit. Universität Innsbruck, p. 136.

Brown, M. (2002). "Retrograde processes in migmatites and granulites revisited". In: *J. Metamorph. Geol.* 20.1, pp. 25–40.

Chowanetz, E. (1990). "Der Winnebachmigmatit (Ötztal/Tirol) - Argumente für eine altpaläozoische Anatexis". Diplomarbeit. Universit{ä}t Wien, p. 74.

— (1991). "Strukturelle und geochronologische Argumente für eine altpaläozoische Anatexis im Winnebachmigmatit (Ötztal/Tirol, Österreich)". In: *Mitt. Ges. Geol.- und Bergbaustud. Österreich* 37, pp. 15–35.

Degeling, H. S. (2002). "Zircon equilibria in metamorphic rocks". Dissertation. Australian National University, p. 230.

Dickin, A. P. (2005). *Radiogenic isotope geology*. 2. ed. Cambridge [u.a.]: Cambridge University Press.

Ghent, E. D. and M. Z. Stout (1984). "TiO2 activity in metamorphosed pelitic and basic rocks: principles and applications to metamorphism in southeastern Canadian Cordillera". In: *Contrib. to Mineral. Petrol.* 86.3, pp. 248–255.

Harley, S. L., N. M. Kelly, and A. Moller (2007). "Zircon Behaviour and the Thermal Histories of Mountain Chains". In: *Elements* 3.1, pp. 25–30.

Harrison, T. M., A. Aikman, P. Holden, A. M. Walker, C. McFarlane, D. Rubatto, and E. B. Watson (2005). "Testing the Ti-in-zircon thermometer". In: *AGU Fall Meet. Abstr.*

Hoernes, S. and E. Hoffer (1973). "Der Amphibolitzug des mittleren Ötztals (Tirol)". In: *Veröff. Museum Ferdinandeum Innsbruck* 53, pp. 159–180.

Hoinkes, G. and M. Thöni (1993). "Evolution of the Ötztal-Stubai, Scarl-Campo and Ulten Basement Units". In: *Pre-Mesozoic Geol. Alps*. Ed. by J. F. von Raumer and F. Neubauer. Berlin, Heidelberg: Springer Berlin Heidelberg, pp. 485–494.

Hoinkes, G. (1973). "Die Anatexis des Winnebachgranites (Ötztaler Alpen, Österreich) am Beispiel eines Aufschlusses". In: *TMPM Tschermaks Miner. und Petrogr. Mitteilungen* 20.3, pp. 225–239.

Hoinkes, G., A. Kostner, and M. Thöni (1991). "Petrological constraints for the Eoalpine eclogite facies metamorphism in the Austroalpine Oetztal basement". In: *Miner. Pet.* 43, pp. 237–254.

Hoinkes, G., F. Purtscheller, and J. Schantl (1972). "Zur Petrographie und Genese des Winnebachgranites (Ötztaler Alpen, Tirol)". In: *TMPM Tschermaks Miner. und Petrogr. Mitteilungen* 18, pp. 292–311.

Hoskin, P. W. O. and U. Schaltegger (2003). "The composition of zircon and igneous and metamorphic petrogenesis". In: *Rev. Mineral. Geochemistry* 53.1, pp. 27–62.

Johannes, W. and F. Holtz (1996). *Petrogenesis and experimental petrology of granitic rocks*. Minerals and rocks ; 22. Berlin [u.a.]: Springer.

Klötzli-Chowanetz, E. (2001). "Migmatite des Ötztalkristallins - Petrologie und Geochronologie". Dissertation. Universität Wien, p. 165.

Klötzli-Chowanetz, E., U. Klötzli, and F. Koller (1997). "Lower Ordovician migmatisation in the Ötztal crystalline basement (Eastern Alps , Austria) : linking U-Pb and Pb-Pb dating with zircon morphology". In: *Schweizerische Miner. und Petrogr. Mitteilungen* 77, pp. 315–324.

Kober, B. (1986). "Whole-grain evaporation for 207Pb/206Pb-age-investigations on single zircons using a double-filament thermal ion source". In: *Contrib. to Mineral. Petrol.* 93.4, pp. 482–490.

Kriegsman, L. M. (2001). "Partial melting, partial melt extraction and partial back reaction in anatectic migmatites". In: *Lithos* 56.1, pp. 75–96.

Ludwig, K. R. (2003). "User's Manual for Isoplot 3.00 - A Geochronological Toolkit for Microsoft Excel". In: *Berkeley Geochronol. Cent. Spec. Publ.* 4, p. 71.

— (2009). "SQUID 2: A User's Manual". In: *Berkeley Geochronol. Cent. Spec. Publ.* 5, p. 110.

Mehnert, K. R. (1968). "Migmatites and the Origin of Granitic Rocks. K. R. Mehnert." In: *Elsevier Sci.*

Miller, C. and M. Thöni (1995). "Origin of eclogites from the Austroalpine Ötztal basement (Tirol, Austria): geochemistry and Sm-Nd vs. Rb-Sr isotope systematics". In: *Chem. Geol.* 122.1, pp. 199–225.

Möller, A., P. J. O'Brien, A. Kennedy, and A. Kröner (2003). "Linking growth episodes of zircon and metamorphic textures to zircon chemistry: an example from the ultrahigh-temperature granulites of Rogaland (SW Norway)". In: *Geochronol. Link. Isot. Rec. with Petrol. abd Textures* 220.May 2007, pp. 65–81.

Ohnesorge, T. (1905). "Die vorderen Kühetaier Berge (Hochedergruppe). (Kurzer vorläufiger Bericht über die Aufnahmsresultate in diesem Gebiete)". In: *Verh. Geol. B.-A.* 7, pp. 175–182.

Park, R. G. (1997). *Foundations of Structural Geology*. Routledge.

Pupin, J. (1980). "Zircon and granite petrology". In: *Contrib. to Mineral. Petrol.* 73.3, pp. 207–220.

Rubatto, D. (2002). "Zircon trace element geochemistry: Partitioning with garnet and the link between U-Pb ages and metamorphism". In: *Chem. Geol.* 184.1-2, pp. 123–138.

Rubatto, D. and D. Gebauer (2000). "Use of cathodoluminescence for U–Pb zircon dating by ion microprobe: some examples from the Western Alps." In: *Cathodoluminescence Geosci.* Ed. by M. Pagel, V. Barbin, P. Blanc, and D. Ohnenstetter. Springer Berlin Heidelberg, pp. 373–400.

Schantl, J. (1972). "Feldpetrographische Untersuchungen des Winnebachmigmatits und der angrenzenden Gesteine". Dissertation. Universität Innsbruck.

Schindlmayr, A. (1999). "Granitoids and plutonic evolution of the Ötztal-Stubai massif; a key for understanding the early palaeozoic history of the Austroalpine crystalline basement in the Western Eastern Alps". Dissertation. Universität Salzburg, p. 287.

Schmidt, K., E. Jäger, M. Grünenfelder, and N. Grögler (1967). "Rb-Sr- und U-Pb-Altersbestimmungen an Proben des Ötztalkristallins und des Schneeberger Zuges." In: *Eclog. geol. Helv.* 60, pp. 529–536.

Schweigl, J. (1993). "Kristallingeologische Untersuchungen in den Nauderer Bergen (Westliche Ötztaler Alpen, Tirol)". Diplomarbeit. University of Vienna, p. 87.

Söllner, F. and B. T. Hansen (1987). ""Panafrikanisches" und "kaledonisches" Ereignis im Ötztal-Kristallin der Ostalpen. Rb-Sr und U-Pb Altersbestimmungen an Migmatiten und Metamorphiten". In: *Jahrb. der Geol. Bundesanstalt* 130.4, pp. 529–569.

Spear, F. S., M. J. Kohn, and J. T. Cheney (1999). "P-T paths from anatectic pelites". In: *Contrib. to Mineral. Petrol.* 134.1, pp. 17–32.

Thöni, M. (1981). "Degree and Evolution of the Alpine Metamorphism in the Austroalpine Unit W of the Hohe Tauern in the light of K-Ar and Rb-Sr Age Determinations on Micas". In: *Jahrb. der Geol. Bundesanstalt* 124, pp. 111–174.

— (1999). "A review of geochronological data from the Eastern Alps". In: *Schweizerische Mineral. Und Petrogr. Mitteilungen* 79.1, pp. 209–230.

Thöny, F. M., P. Tropper, F. Schennach, E. Krenn, F. Finger, R. Kaindl, F. Bernhard, and G. Hoinkes (2008). "The metamorphic evolution of migmatites from the Ötztal Complex (Tyrol, Austria) and constraints on the timing of the pre-Variscan high-T event in the Eastern Alps". In: *Swiss J. Geosci.* 101, Suppl, pp. 111–126.

Watson, E. B., D. A. Wark, and J. B. Thomas (2006). "Crystallization thermometers for zircon and rutile". In: *Contrib. to Mineral. Petrol.* 151.4, pp. 413–433.

Yakymchuk, C., M. Brown, T. J. Ivanic, and F. J. Korhonen (2013). "Leucosome distribution in migmatitic paragneisses and orthogneisses: A record of self-organized melt migration and entrapment in a heterogeneous partially-molten crust". In: *Tectonophysics* 603, pp. 136–154.

Zack, T., R. Moraes, and A. Kronz (2004). "Temperature dependence of Zr in rutile: Empirical calibration of a rutile thermometer". In: *Contrib. to Mineral. Petrol.* 148.4, pp. 471–488.

Appendix A. Sample locations

Migmatite body	Coordinates
Hochmoosferner migmatite	N 47° 02′ 32″ E 011° 09′ 56″
Verpeil migmatite	N 47° 00′ 53″ E 010° 47′ 29″
Klopaier migmatite	N 46° 50′ 35″ E 010° 33′ 13″

Table A.1.: Location of the smaller migmatite bodies in the Ötztal complex.

Sample	Coordinates	Lithology
W1400	N 47° 05′ 04,3″ E 011° 04′ 16,8″	Fine-grained mafic veins
W1401	N 47° 05′ 30,2″ E 011° 03′ 14,7″	Granitic dike, emplaced in migmatite
W1402	N 47° 01′ 40,8″ E 011° 03′ 22,1″	Calcsilicate
W1403	N 47° 03′ 59,5″ E 011° 04′ 45,5″	Mica-shist with staurolite and garnet
W1404	N 47° 05′ 08,6″ E 011° 03′ 54,9″	Neosome, Network & Bubbles
W1405	N 47° 05′ 07,7″ E 011° 03′ 55,2″	Green pinnite within neosome
W1406	N 47° 05′ 07,9″ E 011° 03′ 54,7″	Blue pinnite
W1407	N 47° 05′ 05,9″ E 011° 04′ 02,5″	Pinnite with biotite-rim
W1408	N 47° 05′ 03,5″ E 011° 04′ 05,9″	Calcsilicate
W1409	N 47° 05′ 03,4″ E 011° 04′ 13,5″	Calcsilicate
W1410	N 47° 05′ 04,6″ E 011° 04′ 07,0″	″Spotted gneiss″
W1411	N 47° 05′ 08,7″ E 011° 03′ 55,1″	Leucocratic vein within scholle of bt-schist
W1412	N 47° 05′ 08,7″ E 011° 03′ 55,1″	Neosome, Network & Bubbles
W1413	N 47° 05′ 07,8″ E 011° 03′ 54,3″	Scholle with ptygmatically folded, leucocratic vein

Table A.2.: Sample locations

Appendix B. Mineral chemistry

	Mg	Al	Na	Si	K	Ca	Ba	Sr	Fe	Ti	Mn
LOD	120	120	70	210	160	100	280	100	210	270	190

Table B.1.: Limits of Detection [ppm] at 15kV, 10nA

Feldspar

MgO	Al_2O_3	K_2O	FeO	Na_2O	CaO	TiO_2	SiO_2	BaO	MnO	SrO	Total	Sample, spot
0	19.765	0.072	0.017	11.49	1.4	0	69.227	0	0.013	0	101.984	W1404Rcb1an11
0	21.394	0.088	0.043	9.682	2.882	0.002	65.778	0	0	0	99.869	W1404Rcb1an12
0.004	20.46	0.091	0.037	11.765	1.377	0.01	68.068	0.031	0	0	101.843	W1404Rcb1an13
0	19.435	0.091	0.066	11.016	0.718	0.025	69.977	0.031	0	0	101.359	W1404Rcb1an26
0	20.235	0.066	0	11.106	1.429	0	68.256	0	0	0	101.092	W1404Rcb1an27
0	19.855	0.083	0	11.279	1.233	0.076	68.338	0	0	0	100.864	W1404Rcb1an28
0	19.745	0.106	0.037	10.15	1.624	0	68.768	0	0.002	0	100.432	W1404Rcb1an32
0.025	19.585	0.086	0.217	11.017	1.132	0.007	67.626	0	0.016	0	99.711	W1404Rcb1an33
0.003	20.474	0.077	0.029	11.622	1.438	0	67.431	0.001	0	0	101.075	W1404Rcb1an34
0	17.919	16.724	0.31	0.074	0	0	68.84	0.067	0	0	103.934	W1404Rcb1an49
0	18.021	16.572	0.645	0.052	0.009	0	68.289	0.072	0.004	0	103.664	W1404Rcb1an50
0	17.926	16.624	0.643	0.093	0.004	0.01	67.406	0.137	0.006	0	102.849	W1404Rcb1an51
0.007	19.292	0.077	0.032	11.645	0.972	0.002	69.537	0.043	0	0	101.607	W1404Rcb1an8
0	19.39	0.089	0.021	11.464	0.766	0.027	70.099	0	0	0	101.856	W1404Rcb1an9
0	22.311	0.098	0.005	9.335	3.553	0	64.155	0	0.005	0	99.462	W1410ban10
0	22.132	0.086	0.011	10.063	3.408	0	64.141	0	0	0	99.841	W1410ban8
0	21.249	0.069	0.033	10.186	2.707	0	64.534	0.017	0.024	0	98.819	W1410ban9
0	22.807	0.105	0.126	9.839	4.188	0.025	61.884	0	0.008	0	98.982	W1412Na1ssan10
0.003	20.157	0.06	0.093	11.633	1.078	0.045	65.169	0	0.007	0	98.245	W1412Na1ssan11
0	22.715	0.091	0.102	9.682	4.22	0.003	61.076	0	0	0	97.889	W1412Na1ssan12

Table B.2.: EMPA measurements of feldspars

Muscovite

MgO	Al_2O_3	K_2O	FeO	Na_2O	CaO	TiO_2	SiO_2	BaO	MnO	SrO	Total	Sample, spot
0,977	33,799	10,217	1,163	0,392	0,021	0,086	47,036	0,461	0,003	0	94,155	W1402an11
1,601	32,068	10,59	1,57	0,283	0,023	0,175	48,156	0,193	0,007	0	94,666	W1402an10
1,833	31,02	10,449	1,526	0,225	0,012	0,154	49,242	0,179	0,003	0	94,643	W1402an12
0,814	33,923	10,553	0,969	0,358	0,116	0,461	47,24	0,102	0,02	0	94,556	W1404Rcb1an10
0,564	34,782	10,549	1,066	0,339	0	0,68	47,305	0,174	0,036	0	95,495	W1404Rcb1an55
0,664	34,485	10,814	1,039	0,412	0,031	0,288	47,394	0,096	0,037	0	95,26	W1404Rcb1an57
1,189	32,198	10,641	2,47	0,261	0,008	1,505	47,604	0,161	0,012	0	96,049	W1404Rcb1an52
0,642	34,712	10,577	1,094	0,488	0	0,325	47,667	0,148	0	0	95,653	W1404Rcb1an14
0,61	34,895	10,549	1,041	0,416	0,027	0,14	47,785	0,046	0	0	95,509	W1404Rcb1an56
0,624	34,672	10,59	1,166	0,51	0	0,266	47,963	0,168	0	0	95,959	W1404Rcb1an15
0,573	34,442	10,742	1,057	0,511	0,012	0,267	48,094	0,09	0	0	95,788	W1404Rcb1an16
0,633	34,736	10,625	1,113	0,417	0,01	0,074	48,32	0,007	0,017	0	95,952	W1404Rcb1an30
2,645	28,042	10,643	4,807	0,171	0,005	0,029	48,492	0,651	0,027	0	95,512	W1404Rcb1an25
2,084	29,161	10,536	2,982	0,202	0,085	0,123	48,502	0,876	0,016	0	94,567	W1404Rcb1an24
1,845	30,188	10,838	3,31	0,218	0,032	0,417	48,57	0,373	0,024	0	95,815	W1404Rcb1an20
2,128	28,939	10,661	3,603	0,258	0,013	0,264	48,644	0,515	0,05	0	95,075	W1404Rcb1an22
0,74	34,711	10,693	1,141	0,36	0,008	0,115	48,77	0,177	0,056	0	96,771	W1404Rcb1an31
0,881	33,48	10,686	2,091	0,355	0,029	0,787	48,793	0,203	0,004	0	97,309	W1404Rcb1an54
0,797	33,719	10,598	1,241	0,356	0,026	0,593	48,886	0,126	0,063	0	96,405	W1404Rcb1an3
2,233	28,79	10,714	4,808	0,17	0,001	0,122	49,014	0,642	0,052	0	96,546	W1404Rcb1an23
1,648	31,534	10,071	2,558	0,269	0,094	0,408	49,076	0,121	0,011	0	95,79	W1404Rcb1an1
2,001	28,752	10,78	2,863	0,172	0,01	2,272	49,291	0,168	0,007	0	96,316	W1404Rcb1an53
0,721	33,819	10,753	1,266	0,411	0,012	0,494	49,597	0,101	0,007	0	97,181	W1404Rcb1an7
2,503	29,243	10,548	4,589	0,241	0,017	0,314	49,671	0,629	0,045	0	97,8	W1404Rcb1an21
0,878	34,408	10,772	1,298	0,478	0,028	0,334	50,574	0,161	0	0	98,931	W1404Rcb1an2
1,248	32,114	10,731	1,784	0,362	0,01	0,086	51,103	0,115	0	0	97,553	W1404Rcb1an29
0,499	36,393	10,128	0,956	0,375	0,001	0,345	44,444	0,621	0,000	0,000	93,761	W1406-01an22
0,641	37,160	10,203	1,250	0,297	0,012	0,048	45,355	0,325	0,001	0,000	95,293	W1406-01an21

0,719	36,884	10,005	1,197	0,363	0,007	0,009	45,395	0,307	0,000	0,000	94,885	W1406-01an23
0,672	33,966	10,396	0,949	0,385	0,006	0,519	46,717	0,372	0,005	0	93,987	W1406-01an8
0,604	34,198	10,582	1,052	0,419	0,005	0,644	46,75	0,29	0,013	0	94,557	W1406-01an5
0,655	34,368	10,383	0,943	0,391	0	0,554	46,806	0,372	0	0	94,472	W1406-01an9
0,868	33,545	10,676	1,109	0,447	0,006	0,816	47,62	0,308	0,014	0	95,409	W1406-01an7
0,642	34,282	10,714	1,08	0,453	0,013	0,79	47,938	0,255	0,01	0	96,177	W1406-01an6
1,59	30,442	10,452	2,466	0,296	0,006	0,623	48,733	0,265	0	0	94,873	W1406-01an10
0,824	37,069	10,025	1,573	0,344	0,036	0,074	44,435	0,300	0,024	0,000	94,703	W1407a1-2an2
0,605	37,157	10,010	1,072	0,364	0,025	0,497	45,061	0,086	0,015	0,000	94,892	W1407a1-2an10
0,653	36,890	10,215	0,993	0,319	0,018	0,588	45,114	0,072	0,019	0,000	94,882	W1407a1-2an11
0,907	35,563	9,788	1,453	0,352	0,369	0,031	45,148	0,149	0,007	0,000	93,767	W1407a1-2an3
0,684	36,445	10,055	1,025	0,298	0,019	0,516	45,249	0,073	0,000	0,000	94,364	W1407a1-2an12
1,379	31,839	10,654	2,053	0,263	0,035	0,038	46,017	0,114	0	0	92,392	W1407a1-2an23
0,909	37,642	10,148	1,589	0,293	0,079	0,052	46,083	0,203	0,015	0,000	97,014	W1407a1-2an1
1,388	32,156	10,675	1,877	0,326	0,008	0	46,491	0,125	0	0	93,046	W1407a1-2an22
1,163	33,642	10,788	1,787	0,282	0,035	0,048	47,048	0,145	0,008	0	94,946	W1407a1-2an24
0,822	32,979	10,517	1,708	0,356	0,026	1,085	44,853	0,137	0,042	0	92,525	W1412Na1ssan7
0,718	33,354	10,375	1,124	0,334	0,031	1,406	44,865	0,196	0,011	0	92,414	W1412Na1ssan8
0,573	33,98	10,581	1,488	0,373	0,01	1,102	45,621	0,15	0	0	93,878	W1412Na1ssan9
0,731	34,228	10,259	1,671	0,346	0,005	0,378	47,682	0,178	0,005	0	95,483	W1412Na1ssan31

Table B.3.: EMPA measurements of White Micas

Biotite

MgO	Al_2O_3	K_2O	FeO	Na_2O	CaO	TiO_2	SiO_2	BaO	MnO	SrO	Total	Sample, spot
8,769	18,336	9,441	22,773	0,071	0	1,706	35,922	0,078	0,216	0	97,312	W1404Rcb1an17
8,66	18,72	9,463	22,543	0,13	0	1,739	36,224	0,116	0,259	0	97,854	W1404Rcb1an18
8,711	18,256	9,458	22,335	0,093	0	1,53	36,713	0,081	0,167	0	97,344	W1404Rcb1an19
8,764	18,21	8,831	22,666	0,05	0,062	1,575	34,777	0,103	0,191	0	95,229	W1404Rcb1an35
8,863	18,15	9,482	22,784	0,052	0	1,497	36,064	0,04	0,178	0	97,11	W1404Rcb1an36
8,838	18,629	9,026	22,868	0,099	0,021	1,636	35,698	0,097	0,215	0	97,127	W1404Rcb1an37
8,45	18,314	9,061	22,061	0,074	0,038	1,705	35,079	0	0,245	0	95,027	W1404Rcb1an38
8,802	18,227	8,784	22,101	0,102	0,063	1,787	35,653	0,092	0,216	0	95,827	W1404Rcb1an39
8,706	18,332	9,285	22,164	0,085	0,118	1,609	35,872	0,087	0,213	0	96,471	W1404Rcb1an4
8,72	18,134	9,282	21,882	0,138	0,051	1,759	36	0,123	0,213	0	96,302	W1404Rcb1an40
8,863	17,686	8,19	22,296	0,069	0,163	1,557	36,169	0,084	0,22	0	95,297	W1404Rcb1an41
8,885	17,517	8,415	22,631	0,056	0,055	1,486	37,414	0,073	0,158	0	96,69	W1404Rcb1an42
8,549	18,179	9,093	22,457	0,094	0,073	1,614	35,336	0,008	0,198	0	95,601	W1404Rcb1an43
8,944	17,812	5,486	22,55	0,04	0,542	1,476	35,367	0,038	0,285	0	92,54	W1404Rcb1an44
8,634	17,791	9,178	22,645	0,109	0,02	1,696	36,233	0,074	0,288	0	96,668	W1404Rcb1an48
9,173	17,892	7,792	23,154	0,111	0,079	1,701	35,539	0,161	0,232	0	95,834	W1404Rcb1an5
8,902	18,63	9,767	22,899	0,123	0	2,042	38,462	0,158	0,261	0	101,244	W1404Rcb1an6
8,656	18,222	9,572	22,549	0,078	0	2,091	36,755	0,071	0,227	0	98,221	W1404Rcb1an6rip
8,807	18,373	9,206	21,557	0,188	0	1,878	36,031	0,051	0,113	0	96,204	W1406-01an1
8,674	17,66	9,324	21,595	0,147	0,029	1,831	34,894	0,11	0,129	0	94,393	W1406-01an11
8,797	18,391	9,401	21,96	0,092	0	2,009	35,26	0,104	0,168	0	96,182	W1406-01an12
9,156	17,805	9,085	22,317	0,142	0,011	2,458	34,502	0,2	0,205	0	95,881	W1406-01an14
8,867	18,333	9,215	21,705	0,197	0	1,913	36,627	0,155	0,112	0	97,124	W1406-01an2
8,767	18,621	8,978	21,256	0,197	0,015	2,362	36,277	0,154	0,126	0	96,753	W1406-01an3
8,847	18,084	9,004	20,896	0,207	0	3,267	36,159	0,105	0,167	0	96,736	W1406-01an4
9,669	19,760	8,762	20,839	0,129	0,000	1,108	34,398	0,078	0,092	0,000	94,836	W1407a1-2an4
9,838	19,775	8,782	20,407	0,117	0,000	1,286	35,240	0,078	0,084	0,000	95,608	W1407a1-2an5
9,814	19,817	8,676	19,953	0,130	0,021	1,266	34,967	0,061	0,098	0,000	94,803	W1407a1-2an6

8,61	18,843	8,869	22,516	0,157	0	1,472	36,025	0,076	0,103	0	96,671	W1410ban1
8,894	18,694	8,821	22,601	0,126	0,011	1,645	35,375	0,014	0,061	0	96,242	W1410ban11
8,868	18,562	8,806	22,769	0,151	0	1,586	35,678	0,084	0,065	0	96,569	W1410ban12
9,194	18,527	8,29	22,72	0,163	0	1,642	35,873	0,008	0,116	0	96,533	W1410ban13
9,007	18,207	8,859	22,341	0,155	0	1,757	35,336	0,126	0,074	0	95,862	W1410ban14
8,99	18,658	9,011	22,309	0,174	0	1,801	35,77	0,136	0,058	0	96,907	W1410ban15
9,115	18,471	8,564	22,512	0,112	0	1,686	34,973	0,123	0,094	0	95,65	W1410ban16
8,888	18,753	8,589	22,27	0,127	0,02	1,443	35,292	0,086	0,093	0	95,561	W1410ban2
8,758	18,624	8,753	22,047	0,157	0,004	1,418	34,928	0,083	0,089	0	94,861	W1410ban3
8,92	17,896	9,174	21,137	0,05	0,042	1,452	35,522	0,145	0,167	0	94,505	W1412Na1ssan1
9,448	17,258	9,387	21,652	0,067	0,008	1,658	36,017	0,087	0,185	0	95,767	W1412Na1ssan13
8,988	17,833	9,262	21,577	0,062	0,055	1,639	34,919	0,278	0,203	0	94,816	W1412Na1ssan14
9,199	18,381	7,987	21,246	0,118	0,155	1,602	34,972	0,234	0,191	0	94,085	W1412Na1ssan15
9,189	17,154	7,556	21,644	0,14	0,303	1,277	34,159	0,113	0,217	0	91,752	W1412Na1ssan19
8,827	17,962	9,068	22,547	0,134	0,048	1,779	34,668	0,116	0,221	0	95,37	W1412Na1ssan2
9,201	17,806	9,272	21,515	0,065	0,014	1,358	35,02	0,099	0,238	0	94,588	W1412Na1ssan20
9,117	17,983	9,283	21,647	0,043	0,011	1,651	34,539	0,224	0,182	0	94,68	W1412Na1ssan21
8,643	17,862	8,491	20,408	0,062	0,157	1,726	36,978	0,089	0,166	0	94,582	W1412Na1ssan23
8,524	18,317	8,481	21,68	0,103	0,184	1,484	35,454	0,063	0,226	0	94,516	W1412Na1ssan24
8,731	17,967	9,154	21,606	0,072	0,026	1,502	36,109	0,171	0,187	0	95,525	W1412Na1ssan25
8,984	18,337	9,277	21,763	0,14	0,015	1,626	35,175	0,115	0,19	0	95,622	W1412Na1ssan3
8,848	18,091	9,321	21,632	0,099	0,038	1,738	34,82	0,097	0,188	0	94,872	W1412Na1ssan4
8,926	17,922	9,089	21,843	0,097	0	1,639	35,028	0,059	0,243	0	94,846	W1412Na1ssan5
8,957	18,352	9,124	21,716	0,094	0,018	1,644	34,787	0,161	0,17	0	95,023	W1412Na1ssan6

Table B.4.: EMPA measurements of biotite

Garnet

MgO	Al_2O_3	K_2O	FeO	Na_2O	CaO	TiO_2	SiO_2	BaO	MnO	SrO	Total	Sample, spot
3,494	21,558	0,022	32,467	0,001	0,939	0,008	35,967	0,000	5,067	0,000	99,523	W1407a1-2an15
3,199	21,567	0,025	32,464	0,000	1,026	0,064	36,113	0,000	5,154	0,000	99,612	W1407a1-2an14
2,578	21,168	0,013	33,051	0,009	1,176	0,004	36,120	0,000	5,720	0,000	99,838	W1407a1-2an16
3,929	21,914	0,024	32,786	0,005	0,901	0,006	36,396	0,000	4,017	0,000	99,979	W1407a1-2an17
3,970	21,956	0,002	32,982	0,024	0,821	0,000	36,829	0,000	4,638	0,000	101,222	W1407a1-2an13
5,192	21,547	0,028	33,469	0,039	0,987	0,000	38,021	0,000	2,940	0,000	102,223	W1407a1-2an18
2,689	21,295	0,014	37,642	0,000	1,223	0,023	37,584	0,000	3,546	0,000	104,016	W1410ban6
2,465	21,476	0,038	37,273	0,000	1,105	0,000	38,064	0,000	3,424	0,000	103,845	W1410ban7
2,392	21,006	0,321	32,993	0,000	2,060	0,000	37,532	0,019	4,761	0,000	101,084	W1412Na1ssan16
2,860	21,242	0,001	32,357	0,021	3,150	0,023	37,686	0,000	4,215	0,000	101,555	W1412Na1ssan18
2,674	20,475	0,019	32,288	0,008	3,368	0,018	37,763	0,000	4,160	0,000	100,773	W1412Na1ssan17

Table B.5.: EMPA measurements of garnets

Amphibole

MgO	Al_2O_3	K_2O	FeO	Na_2O	CaO	TiO_2	SiO_2	BaO	MnO	SrO	Total	Sample, spot
16,609	2,083	0,045	10,805	0,169	12,003	0,048	55,552	0,000	0,349	0,000	97,663	W1408aan5, actinolite

Table B.6.: EMPA measurements of amphiboles

Appendix C. Thermometry

	Si	Ca	Ti	Y	Zr	La	Ce	Yb	Hf	P
LOD	250	105	43	178	704	231	196	297	293	275

Table C.1.: Limits of Detection [ppm] at 20kV, 30nA

	Ti	Zr	Hf	K
LOD	17	770	180	138

Table C.2.: Limits of Detection [ppm] at 15kV, 100nA

Sample, spot	TiO_2 [wt%]	Ti [ppm]	Det. limit [ppm]	T [°C]	Error [°C]
W1412Hn2_ov01_zrk08	0,0044	9,4	43	735,3	191,0
W1404LaN1_ov02-zrk01	0,0056	16,6	43	787,4	154,8
W1404LaN1_ov01-zrk07	0,0062	20,2	43	806,6	143,0
W1404LaN1_ov02-zrk04	0,0062	20,2	43	806,6	143,0
W1412Hn2_ov01_zrk07	0,0062	20,2	43	806,6	143,0
W1404LaN1_ov02-zrk05	0,007	25,0	43	828,3	130,7
W1412Nab1-zrk07	0,0073	26,8	43	835,5	126,8
W1412Hn2_ov01_zrk02	0,0079	30,4	43	849,0	120,0
W1412Hn2_ov01_zrk17	0,0079	30,4	43	849,0	120,0
W1412Hn2_ov01_zrk02	0,0081	31,6	43	853,1	117,9
W1412Hn2_ov01_zrk07	0,0081	31,6	43	853,1	117,9
W1412Hn2_ov2_zrk02	0,0056	33,6	17	859,9	62,1
W1412Hn1_ov01-zrk08	0,0094	39,3	43	877,6	106,7
W1412Hn2_ov01_zrk03	0,0095	39,9	43	879,3	105,9
W1412Hn2_ov2_zrk02	0,0075	45,0	17	892,9	54,3
W1412Hn2_ov01_zrk03	0,0113	50,7	43	907,1	94,8
W1404LaN2_ov01-zrk08	0,0131	61,5	43	930,5	86,6
W1412Nab1-zrk08	0,0133	62,7	43	932,9	85,9
W1412Nab1-zrk06	0,0166	82,5	43	968,0	75,6
W1404LaN1_ov01-zrk10	0,0169	84,3	43	970,8	74,8
W1404LaN1_ov01-zrk12	0,018	90,9	43	980,9	72,3
W1404LaN2_ov01-zrk04	0,0183	92,7	43	983,5	71,6
W1412Hn2_ov01_zrk10	0,019	96,9	43	989,5	70,2
W1412Hn1_ov01-zrk06	0,0198	101,7	43	996,1	68,7
W1412Hn2_ov1_zrk22	0,0182	109,1	17	1005,9	38,4
W1404LaN1_ov01-zrk12	0,0214	111,3	43	1008,7	66,0
W1407b3_ov02-zrk04	0,0222	116,1	43	1014,6	64,8
W1412Hn2_ov01_zrk10	0,0222	116,1	43	1014,6	64,8
W1412Hn2_ov01_zrk10	0,0225	117,9	43	1016,8	64,4
W1404LaN2_ov01-zrk09	0,0229	120,3	43	1019,7	63,8
W1404LaN1_ov01-zrk12	0,0202	121,1	17	1020,6	37,1
W1412Hn1_ov01-zrk04	0,0244	129,3	43	1030,0	61,9
W1412Hn2_ov2_zrk03	0,0217	130,1	17	1031,0	36,4
W1404LaN1_ov03-zrk04	0,0253	134,6	43	1036,0	60,8
W1404LaN1_ov01-zrk08	0,0256	136,4	43	1038,0	60,5
W1412Hn2_ov01_zrk01	0,0258	137,6	43	1039,2	60,2
W1412Hn2_ov01_zrk10	0,0241	144,5	17	1046,4	35,3
W1412Nab1-zrk11	0,0279	150,2	43	1052,3	58,1
W1412Hn2_ov2	0,0295	176,8	17	1077,2	33,7

Table C.3.: Thermometry data, sorted in ascending Temperature

Appendix D. Geochronological data

Spot	232Th /238U	ppm U	ppm Th	Th/U
1.1	0,34	206,72	67,44	0,33
2.2	0,30	668,11	192,02	0,29
2.3	0,12	352,23	39,45	0,11
2.7	0,45	1007,34	443,14	0,44
4.1	2,06	367,19	730,59	1,99
01a		409,20	150,80	0,37
02a		1078,50	576,50	0,53
03a		532,30	118,60	0,22
03b		402,30	97,70	0,24
04a		717,60	24,40	0,03
04b		605,20	42,90	0,07
05a		1693,40	-	-
05b		441,50	50,80	0,12
06a		840,50	66,20	0,08
06b		664,90	57,80	0,09
07a		314,20	119,90	0,38
08a		423,40	34,60	0,08
09a		231,40	31,00	0,13
10a		463,70	37,20	0,08
11a		241,40	-	-

Table D.1.: Th/U ratios of zircons from the Gaislehn granitic gneiss and zircons from the Winnebach migmatite (first five spots) yielding the corresponding concordia-age. Data of Gaislehn zircons from Klötzli-Chowanetz (2001).

Spot	Bkrd Cts/sec	total 196 Cts/sec	total 204 Cts/sec	total 206 Cts/sec	204 /206	% err	207 /206	% err
8.1	0,367	238653,454	0,343	5693,493	0,000	83,205	0,111	0,544
8.2	0,267	139334,981	0,367	429,699	0,000	40,828	0,066	4,451
9.1	0,200	202579,831	0,283	2081,151	0,000	44,722	0,130	0,751
10.1	0,433	148597,758	0,567	1336,681	0,000	35,357	0,058	2,712
10.2	0,633	254806,584	2,056	6124,561	0,000	15,130	0,076	2,269
6.1	0,450	182880,237	0,511	3606,038	0,000	52,224	0,060	1,562
4.1	0,533	144562,474	0,570	1114,773	0,000	67,083	0,061	2,736
4.2	0,450	167919,972	0,661	3458,886	0,000	28,098	0,059	0,949
5.1	0,167	139047,723	4,183	445,148	0,012	9,773	0,242	12,746
1.1	0,317	216278,050	0,550	1206,381	0,000	26,728	0,062	2,599
2.1	0,450	201455,816	1,870	4196,076	0,000	28,820	0,063	0,789
2.3	0,233	194396,106	0,600	1548,481	0,000	21,322	0,058	2,462
2.2	0,517	169167,460	1,278	2654,571	0,000	37,742	0,062	1,773
2.5	0,283	128901,832	13,209	1269,892	0,014	5,596	0,240	2,502
2.7	0,663	165699,338	0,743	4307,977	0,000	45,750	0,059	3,883
3.1	0,494	164291,545	0,700	979,507	0,000	28,477	0,061	2,974

Table D.2.: SHRIMP measurements of zircons

Spot	208 /206	% err	238 /196	% err	206 /238	% err	254 /238	% err	248 /254	% err	206 /254	% err
8.1	0,027	2,027	0,055	6,760	0,430	0,844	4,971	1,618	0,092	1,918	0,086	1,180
8.2	0,167	2,997	0,015	5,867	0,204	1,836	5,032	1,519	0,486	1,703	0,040	0,954
9.1	0,004	4,367	0,018	1,727	0,556	4,862	4,666	2,136	0,015	2,259	0,119	2,880
10.1	0,502	1,025	0,058	2,975	0,151	4,577	4,715	1,432	1,393	2,490	0,032	2,929
10.2	0,091	0,493	0,121	2,863	0,197	5,643	4,752	2,359	0,215	2,409	0,041	2,851
6.1	0,211	0,956	0,107	2,421	0,185	1,151	5,441	0,626	0,709	2,393	0,034	1,391
4.1	0,651	0,517	0,043	3,966	0,180	3,110	5,187	0,942	2,025	0,887	0,034	2,013
4.2	0,067	4,734	0,161	3,519	0,126	7,710	4,649	3,418	0,177	2,523	0,026	4,947
5.1	0,500	14,485	0,019	2,172	0,162	4,966	4,971	1,032	0,283	1,679	0,032	3,806
1.1	0,109	2,052	0,036	0,497	0,154	2,959	4,827	0,990	0,321	0,515	0,032	2,100
2.1	0,047	1,694	0,135	4,150	0,152	6,003	4,904	3,002	0,129	1,019	0,031	2,415
2.3	0,037	3,042	0,063	2,016	0,126	4,931	4,547	1,403	0,114	1,026	0,027	3,336
2.2	0,097	1,492	0,128	3,395	0,121	6,907	4,424	2,235	0,273	1,515	0,027	4,530
2.5	0,536	3,888	0,056	2,109	0,173	6,298	4,862	1,459	0,156	1,332	0,035	4,726
2.7	0,142	0,960	0,171	0,486	0,149	5,016	4,689	1,950	0,408	1,670	0,031	2,855
3.1	0,266	1,649	0,035	1,430	0,168	3,937	4,778	1,721	0,859	1,196	0,035	2,141

SHRIMP measurements of zircons (continued)

Spot	206Pb /238U calibr. const	% err	7-corr 204Pb /206Pb	8-corr 204Pb /206Pb	4-corr %com 206
8.1	0,015	3,177	0,002	0,000	-0,008
8.2	0,008	1,251	0,000	0,000	0,420
9.1	0,026	4,285	0,000	0,000	0,072
10.1	0,007	1,493	0,000	0,000	0,180
10.2	0,009	2,010	0,001	0,001	0,813
6.1	0,006	0,191	0,000	0,000	0,031
4.1	0,007	1,736	0,000	0,001	0,060
4.2	0,005	13,016	0,000	0,000	0,110
5.1	0,007	3,487	0,013	0,011	22,124
1.1	0,007	0,309	0,000	0,000	0,349
2.1	0,006	2,940	0,000	0,000	0,530
2.3	0,007	1,339	0,000	0,000	0,428
2.2	0,007	1,633	0,000	0,000	0,564
2.5	0,008	0,608	0,012	0,013	24,619
2.7	0,007	2,077	0,000	0,000	0,033
3.1	0,007	1,372	0,000	0,000	0,379

SHRIMP measurements of zircons (continued)

Spot	7-corr %com 206	8-corr %com 206	4-corr %com 208	7-corr %com 208	4-corr 208Pb* /206Pb*	% err
8.1	3,593	-0,056	-0,592	278,813	0,027	2,072
8.2	0,441	-0,006	5,263	5,516	0,159	3,794
9.1	0,356	-0,004	34,527	169,926	0,003	24,478
10.1	-0,342	0,597	0,753	-1,431	0,499	1,053
10.2	1,418	1,388	18,665	32,538	0,075	3,402
6.1	0,104	0,135	0,304	1,031	0,211	0,970
4.1	0,115	1,112	0,193	0,371	0,650	0,526
4.2	0,400	0,316	3,424	12,420	0,065	4,996
5.1	22,946	20,301	92,846	96,298	0,046	237,475
1.1	0,218	0,226	6,748	4,203	0,102	2,868
2.1	0,480	0,299	23,591	21,371	0,036	9,021
2.3	-0,239	0,073	24,068	-13,438	0,028	7,778
2.2	0,227	0,265	12,199	4,910	0,086	5,309
2.5	22,465	23,724	96,279	87,854	0,026	177,085
2.7	-0,241	0,095	0,493	-3,554	0,141	0,988
3.1	-0,134	0,165	2,986	-1,057	0,259	1,865

SHRIMP measurements of zircons (continued)

Spot	7-corr 208Pb* /206Pb*	% err	ppm U	ppm Th	4-corr ppm 206*	7-corr ppm 206*	8-corr ppm 206*
8.1	-0,050	15,451	421,643	38,724	81,444	78,512	81,484
8.2	0,159	5,677	121,748	64,236	11,627	11,624	11,676
9.1	-0,003	521,871	181,721	2,768	58,807	58,640	58,852
10.1	0,507	1,256	648,045	1001,705	57,861	58,164	57,619
10.2	0,063	9,283	1155,291	230,842	127,222	126,447	126,485
6.1	0,209	1,570	1009,454	658,925	80,151	80,092	80,067
4.1	0,649	0,773	367,190	730,586	31,808	31,791	31,474
4.2	0,059	31,356	1482,553	281,439	91,697	91,432	91,509
5.1	0,024	581,335	186,904	54,151	13,273	13,133	13,584
1.1	0,104	4,477	206,719	67,444	17,645	17,669	17,667
2.1	0,037	12,651	631,901	80,926	49,223	49,248	49,338
2.3	0,042	10,418	352,235	39,454	29,395	29,592	29,499
2.2	0,092	4,352	668,111	192,023	56,909	57,102	57,081
2.5	0,084	39,499	293,510	46,669	23,476	24,147	23,755
2.7	0,147	4,443	1007,342	443,142	89,281	89,526	89,226
3.1	0,269	2,369	194,023	160,671	18,328	18,422	18,367

SHRIMP measurements of zircons (continued)

Spot	4-corr ppm 208*	7-corr ppm 208*	232Th /238U	% err	Total 206Pb /238U	% err	Total 208Pb /232Th	% err
8.1	2,235	-3,974	0,095	0,243	0,225	3,323	0,064	3,900
8.2	1,871	1,866	0,545	1,190	0,112	1,586	0,034	3,593
9.1	0,171	-0,182	0,016	2,457	0,377	4,394	0,105	6,664
10.1	29,152	29,794	1,597	1,202	0,104	1,782	0,033	2,382
10.2	9,626	7,984	0,206	1,513	0,129	2,234	0,057	2,742
6.1	17,044	16,920	0,674	1,189	0,092	0,993	0,029	1,820
4.1	20,870	20,833	2,055	0,688	0,101	1,991	0,032	2,169
4.2	6,042	5,479	0,196	4,601	0,072	13,052	0,025	14,627
5.1	0,615	0,318	0,299	2,088	0,106	3,620	0,177	15,076
1.1	1,810	1,859	0,337	0,860	0,100	0,588	0,032	2,301
2.1	1,798	1,850	0,132	0,815	0,091	2,983	0,032	3,526
2.3	0,843	1,260	0,116	0,296	0,098	1,430	0,031	3,374
2.2	4,920	5,328	0,297	1,107	0,100	1,708	0,033	2,523
2.5	0,627	2,048	0,164	0,317	0,124	0,787	0,403	3,980
2.7	12,740	13,258	0,454	0,968	0,103	2,136	0,032	2,534
3.1	4,797	4,997	0,855	0,909	0,110	1,460	0,034	2,383

SHRIMP measurements of zircons (continued)

Spot	204corr 206Pb /238U Age	1s err	207corr 206Pb /238U Age	1s err	208corr 206Pb /238U Age	1s err
8.1	1307,535	39,326	1264,784	40,712	1308,113	39,825
8.2	679,555	10,286	679,424	10,745	682,314	11,303
9.1	2060,989	77,510	2055,983	93,438	2062,343	77,698
10.1	637,466	10,826	640,643	11,177	634,930	14,728
10.2	777,571	16,388	773,105	16,826	773,328	17,024
6.1	569,914	5,415	569,515	5,550	569,342	6,097
4.1	619,362	11,760	619,036	12,064	613,143	17,581
4.2	448,215	56,515	446,959	57,131	447,324	58,280
5.1	512,056	22,457	506,856	30,464	523,571	33,627
1.1	610,713	3,467	611,483	3,697	611,434	3,682
2.1	559,580	16,008	559,848	16,290	560,823	16,385
2.3	597,691	8,177	601,509	8,440	599,721	8,338
2.2	609,491	10,010	611,462	10,202	611,241	10,452
2.5	573,923	10,927	589,598	7,149	580,445	9,586
2.7	633,012	12,881	634,664	13,310	632,641	13,821
3.1	672,553	9,350	675,842	9,705	673,926	10,874

SHRIMP measurements of zircons (continued)

Spot	204corr 207Pb /206Pb Age	1s err	204corr 208Pb /232Th Age	1s err	% Dis- cor- dant	7corr 206* /238	% err
8.1	1814,725	9,912	1262,072	48,087	30,838	0,217	1,131
8.2	685,001	111,160	646,509	27,035	0,838	0,111	0,531
9.1	2084,765	13,668	1346,239	319,185	1,332	0,376	1,693
10.1	485,213	64,693	646,094	15,240	-32,962	0,104	0,585
10.2	923,384	58,963	919,512	39,772	16,759	0,127	0,737
6.1	591,097	34,338	575,264	10,363	3,744	0,092	0,325
4.1	634,784	60,487	634,367	13,570	2,548	0,101	0,652
4.2	537,516	23,093	478,594	69,341	17,197	0,072	4,220
5.1	803,646	1443,768	254,672	323,260	37,732	0,082	1,993
1.1	572,908	65,559	596,429	17,665	-6,917	0,100	0,202
2.1	544,823	49,857	495,133	46,812	-2,828	0,091	0,969
2.3	394,411	66,362	476,430	35,568	-53,979	0,098	0,469
2.2	510,589	78,389	569,866	32,701	-20,303	0,099	0,558
2.5	-583,694	1264,129	301,047	432,841	207,562	0,096	0,405
2.7	554,877	85,250	638,381	15,990	-14,786	0,103	0,702
3.1	526,732	76,416	662,587	16,549	-29,159	0,111	0,482

SHRIMP measurements of zircons (continued)

Spot	4corr 208* /232	% err	Total 238 /206	% err	Total 207 /206	% err	4corr 238 /206*	% err
8.1	0,064	3,930	4,447	3,323	0,111	0,544	4,447	3,323
8.2	0,033	4,249	8,957	1,586	0,066	4,451	8,995	1,595
9.1	0,069	24,508	2,653	4,394	0,130	0,751	2,654	4,394
10.1	0,032	2,397	9,603	1,782	0,058	2,712	9,621	1,784
10.2	0,047	4,424	7,737	2,234	0,076	2,269	7,801	2,237
6.1	0,029	1,827	10,815	0,993	0,060	1,562	10,819	0,993
4.1	0,032	2,173	9,910	1,991	0,061	2,736	9,916	1,991
4.2	0,024	14,661	13,873	13,052	0,059	0,949	13,888	13,052
5.1	0,013	127,734	9,420	3,620	0,242	12,746	12,096	4,562
1.1	0,030	3,006	10,028	0,588	0,062	2,599	10,063	0,595
2.1	0,025	9,571	10,969	2,983	0,063	0,789	11,027	2,987
2.3	0,024	7,554	10,249	1,430	0,058	2,462	10,293	1,433
2.2	0,029	5,820	10,028	1,708	0,062	1,773	10,085	1,721
2.5	0,015	144,852	8,096	0,787	0,240	2,502	10,740	1,990
2.7	0,032	2,544	9,689	2,136	0,059	3,883	9,692	2,136
3.1	0,033	2,539	9,059	1,460	0,061	2,974	9,094	1,464

SHRIMP measurements of zircons (continued)

Spot	4corr 207* /206*	% err	4corr 207* /235	% err	4corr 206* /238	% err	err corr
8.1	0,111	0,546	3,439	3,368	0,225	3,323	0,987
8.2	0,062	5,207	0,955	5,446	0,111	1,595	0,293
9.1	0,129	0,777	6,702	4,462	0,377	4,394	0,985
10.1	0,057	2,930	0,815	3,430	0,104	1,784	0,520
10.2	0,070	2,869	1,234	3,638	0,128	2,237	0,615
6.1	0,060	1,584	0,760	1,869	0,092	0,993	0,531
4.1	0,061	2,810	0,846	3,444	0,101	1,991	0,578
4.2	0,058	1,055	0,578	13,095	0,072	13,052	0,997
5.1	0,066	68,946	0,751	69,096	0,083	4,562	0,066
1.1	0,059	3,014	0,811	3,072	0,099	0,595	0,194
2.1	0,058	2,281	0,730	3,758	0,091	2,987	0,795
2.3	0,055	2,959	0,731	3,287	0,097	1,433	0,436
2.2	0,057	3,566	0,786	3,960	0,099	1,721	0,435
2.5	0,037	46,661	0,470	46,703	0,093	1,990	0,043
2.7	0,059	3,908	0,835	4,454	0,103	2,136	0,480
3.1	0,058	3,486	0,878	3,781	0,110	1,464	0,387

SHRIMP measurements of zircons (continued)

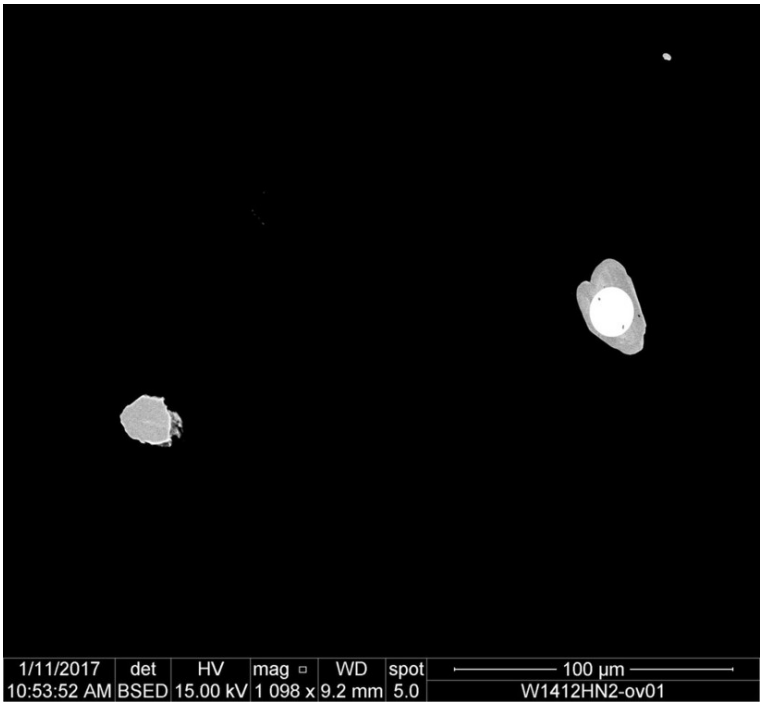

Figure D.1.: SHRIMP spot 2.1; Thermometry spot W1412HN2ov1_ Zrk20

Figure D.2.: SHRIMP spot 2.5; Thermometry spot W1412HN2ov1_ Zrk08

Figure D.3.: SHRIMP spot 2.5; Thermometry spot W1412HN1_ Zrko8

Figure D.4.: SHRIMP spot 4.2; Thermometry spot W1412Nab1_ Zrko8

Figure D.5.: SHRIMP measurement 5.1; Thermometry spot W1404LaN1ov01_ Zrk10

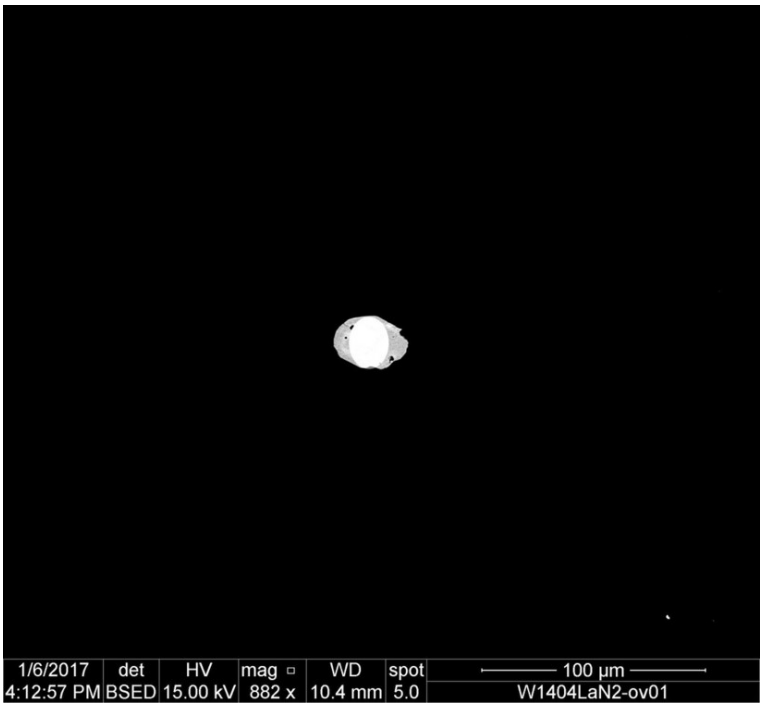

Figure D.6.: SHRIMP measurement 6.1; Thermometry spot W1404LaN2ov01_ Zrk08

Figure D.7.: SHRIMP measurement 8.1; Thermometry below detection limit

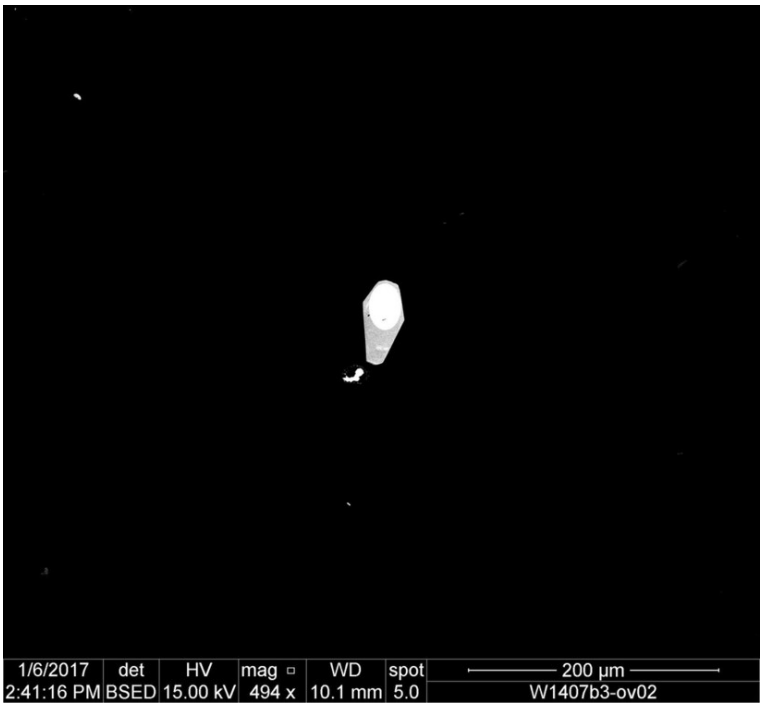

Figure D.8.: SHRIMP measurement 8.2; Thermometry below detection limit

Figure D.9.: SHRIMP measurement 9.1; Thermometry spot W1404Lan10v02_ Zrk05

Figure D.10.: SHRIMP measurement 10.1; Thermometry spot W1404LaN10v03_ Zrk07

Figure D.11.: SHRIMP measurement 10.2; Thermometry spot W1404LaN10v03_ Zrk04

Appendix E. Abstract

The Winnebach migmatite is a polymetamorphic migmatite located in the Ötztal Complex (Eastern Alps, Austria). The partial anatexis is of an Cambro-Ordovician age. Petrological investigations, coupled with geochronological studies were made to further examine the generation of melt. The method of Ti-in-Zircon thermometry was tested for applicability and usefulness.

The multitude of lithologies and textures was found to be in agreement with the migmatite model by Kriegsman (2001): If the melt gets segregated from the restite, a partial back-reaction leads to the formation of melanosome and leucosome, respectively. In the case of the Winnebach migmatite, these are represented by white melt-channels with biotite selvedges, or schollen of biotite schist with coarse grained layers of quartz and feldspar. If the melt stays In-Situ, the partial back-reaction forms the mesosome, which is represented by schollen of bt-pl gneiss, and a granodioritic mass in the Winnebach.

Application of a microprobe for Ti-in-Zircon thermometry limits the method to very high temperature rocks (e.g. granulites), as Ti-contents associated with lower temperatures lie below detection limits.

Even though the age of the anatexis is only present in a fraction of zircons specific to the migmatite, concordia ages obtained from the Winnebach migmatite can be correlated to the adjacent Gaislehn granitic gneiss. The concordia age of 610 Ma is interpreted as the age of intrusion of the Gaislehn granite.

Zusammenfassung

Der Winnebach Migmatit ist ein polymetamorpher Migmatitkörper im Ötztal Komplex (Ostalpen, Österreich). Die partielle Anatexis hat ein Kambro-ordovizisches Alter. Petrologische Untersuchungen, in Verbindung mit geochronologischen Studien wurden durchgeführt um die entstehung der Schmelzen näher zu untersuchen. Die Methode der Ti-in-Zirkon Thermometrie wurde auf Anwendbarkeit und Nützlichkeit untersucht.

Die Vielzahl an Lithologien und Texturen stimmen mit dem Migmatitmodell von Kriegsman (2001) überein: Wenn die Schmelze vom Restit getrennt wird führt eine partielle Rückreaktion zu der Bildung von Melanosom, beziehungsweise Leukosom. Im Fall vom Winnebach Migmatit bedeutet dies weiße Schmelzkanäle mit Biotitsäumen, oder Schollen aus Biotitschiefer mit grobkörnigen Quarz-Feldspat Lagen. Wenn die Schmelzen In-Situ verbleibt wird durch die partielle Rückreaktion das Mesosom gebildet; im Winnebach entweder Schollen von Bt-Pl Gneiß, oder eine granodioritische, unorientierte Masse.

Die Verwendung einer Mikrosonde für Ti-in-Zirkon Thermometrie limitiert diese Methode auf Hochtemperaturgesteine (z.B. Granulite), da die niedrigen Ti-Gehalte, welche niedrige Temperaturen darstellen, unter der Nachweisgrenze liegen.

Obwohl das Alter der Anatexis nur in einer spezifischen Zirkonfraktion im Migmatit festgehalten ist, können Concordiaalter vom Migmatit mit Altern aus dem angrenzenden Gaislehn Granitgneiß korreliert werden. Das Concordiaalter von 610 Ma wird als das Intrusionsalter des Gaislehngranits interpretiert.